

AD _____

Award Number: W81XWH-09-1-0050

TITLE: Integrated Device for Circulating Tumor Cell Capture, Characterization and Lens-Free Microscopy

PRINCIPAL INVESTIGATOR: Richard Cote, PhD

CONTRACTING ORGANIZATION: University of Miami, Miami, FL 33136

REPORT DATE: August 2012

TYPE OF REPORT: Final (Revised)

PREPARED FOR: U.S. Army Medical Research and Materiel Command
Fort Detrick, Maryland 21702-5012

DISTRIBUTION STATEMENT: Approved for Public Release;
Distribution Unlimited

The views, opinions and/or findings contained in this report are those of the author(s) and should not be construed as an official Department of the Army position, policy or decision unless so designated by other documentation.

REPORT DOCUMENTATION PAGE				Form Approved OMB No. 0704-0188	
Public reporting burden for this collection of information is estimated to average 1 hour per response, including the time for reviewing instructions, searching existing data sources, gathering and maintaining the data needed, and completing and reviewing this collection of information. Send comments regarding this burden estimate or any other aspect of this collection of information, including suggestions for reducing this burden to Department of Defense, Washington Headquarters Services, Directorate for Information Operations and Reports (0704-0188), 1215 Jefferson Davis Highway, Suite 1204, Arlington, VA 22202-4302. Respondents should be aware that notwithstanding any other provision of law, no person shall be subject to any penalty for failing to comply with a collection of information if it does not display a currently valid OMB control number. PLEASE DO NOT RETURN YOUR FORM TO THE ABOVE ADDRESS.					
1. REPORT DATE August-2012		2. REPORT TYPE Revised FINAL		3. DATES COVERED 1 Aug 2009 – 31 July 2012	
4. TITLE AND SUBTITLE Integrated Device for Circulating Tumor Cell Capture, Characterization and Lens-Free Microscopy				5a. CONTRACT NUMBER	
				5b. GRANT NUMBER W81XWH-09-1-0050	
				5c. PROGRAM ELEMENT NUMBER	
6. AUTHOR(S) Richard Cote, Changhui Yang, Ram Datar E-Mail: RCote@med.miami.edu				5d. PROJECT NUMBER	
				5e. TASK NUMBER	
				5f. WORK UNIT NUMBER	
7. PERFORMING ORGANIZATION NAME(S) AND ADDRESS(ES) University of Miami Miami,, FL 33146				8. PERFORMING ORGANIZATION REPORT NUMBER	
9. SPONSORING / MONITORING AGENCY NAME(S) AND ADDRESS(ES) U.S. Army Medical Research and Materiel Command Fort Detrick, Maryland 21702-5012				10. SPONSOR/MONITOR'S ACRONYM(S)	
				11. SPONSOR/MONITOR'S REPORT NUMBER(S)	
12. DISTRIBUTION / AVAILABILITY STATEMENT Approved for Public Release; Distribution Unlimited					
13. SUPPLEMENTARY NOTES					
14. ABSTRACT The detection of circulating tumor cells (CTC) in the peripheral blood of breast cancer patients indicates high metastatic potential and increased morbidity. Development of a cost-effective CTC detection and imaging system can revolutionize the field of cancer prognosis, therapeutic response monitoring and drug development. Our cell-size-based parylene microfilter platform captures CTC from the cancer patients' blood cost effectively, where the larger CTC are preferentially retained on the membrane while typical blood cells flow through. Our collaborators (Yang et al, Caltech) have simultaneously developed novel wide field-of-view scanning microscope method. In the study supported by this funding, we aimed to integrate our novel CTC capture microfilter system with the wide field-of-view scanning microscope to permit harvesting and analysis of CTC at high resolution. At the conclusion, we have completed the task of achieving tumor cell capture through parylene-based microfiltration technology for breast cancer with high sensitivity (Aim 1), defining imaging parameters for CTC analysis using the microfilter device (Aim 2), development and evaluation of various novel WFOV methods in response to the established parameters (Aim 3), and finally, we have combined the microfiltration and WFOV microscopy components to create an integrated CTC analysis system (Aim 4).					
15. SUBJECT TERMS circulating tumor cells (CTC), parylene microfilter, wide field-of-view scanning microscope					
16. SECURITY CLASSIFICATION OF:			17. LIMITATION OF ABSTRACT	18. NUMBER OF PAGES	19a. NAME OF RESPONSIBLE PERSON
a. REPORT	b. ABSTRACT	c. THIS PAGE			USAMRMC
U	U	U	UU	47	19b. TELEPHONE NUMBER (include area code)

Table of Contents

	<u>Page</u>
Introduction.....	4
Body.....	4
Key Research Accomplishments.....	4
Reportable Outcomes.....	8
Conclusion.....	8
References.....	8
Appendices.....	9

Introduction

This document represents the final report on the progress during this study, from August 2009 – July 30, 2012, towards the work done collaboratively at University of Miami by the researchers led by Drs. Cote and Datar.

Background

The detection of circulating tumor cells (CTC) in the peripheral blood of breast cancer (BC) patients has been an area of interest and investigation over the past 25 years. For with metastatic breast cancer, CTC may indicate high metastatic potential and increased morbidity, and the ability to monitor CTC could provide a real-time assessment of therapeutic efficacy. The development of a cost-effective and high-throughput CTC analysis system would revolutionize the field of CTC detection, prognosis, and therapeutic response monitoring and target development. We have developed a parylene microfilter-based CTC capture device that could revolutionize the capture of CTC from the blood of patients with breast cancer cost effectively. The technology is based on filtering blood through a finely engineered parylene membrane microfilter, where the larger CTC (15-25 μm) are preferentially retained on the membrane while typical blood cells (2-12 μm) flow through. Our collaborators (Yang et al, Caltech) were simultaneously developing a number of novel wide field-of-view scanning microscope methods, from which we then implement the microscope based on the most suitable method for imaging and analyzing tumor cells at a high throughput rate. In the study proposed during this funding, we aimed to integrate our novel CTC capture microfilter system with the wide field-of-view scanning microscope to permit harvesting and analysis of CTC at high resolution, with a potential to arrive at a low cost and high throughput technology. Studies in Aims 1 and a part of Aim 2 were to be conducted at University of Miami, Aim 3 to be conducted at California Institute of Technology, and Aim 4 to be conducted jointly between University of Miami and California Institute of Technology.

Specific Aims

- Aim 1: Adapt the membrane microfilter device for breast CTC capture, Identification and characterization (University of Miami)
- Aim 2: Fully evaluate the microscopy imaging needs associated with using the microfilter device for CTC capture, identification and characterization (University of Miami)
- Aim 3: Implement a wide field-of view (WFOV) high-resolution microscope system (California Institute of Technology)
- Aim 4: Combine these two components to create a high-throughput CTC analysis system (University of Miami and California Institute of Technology)

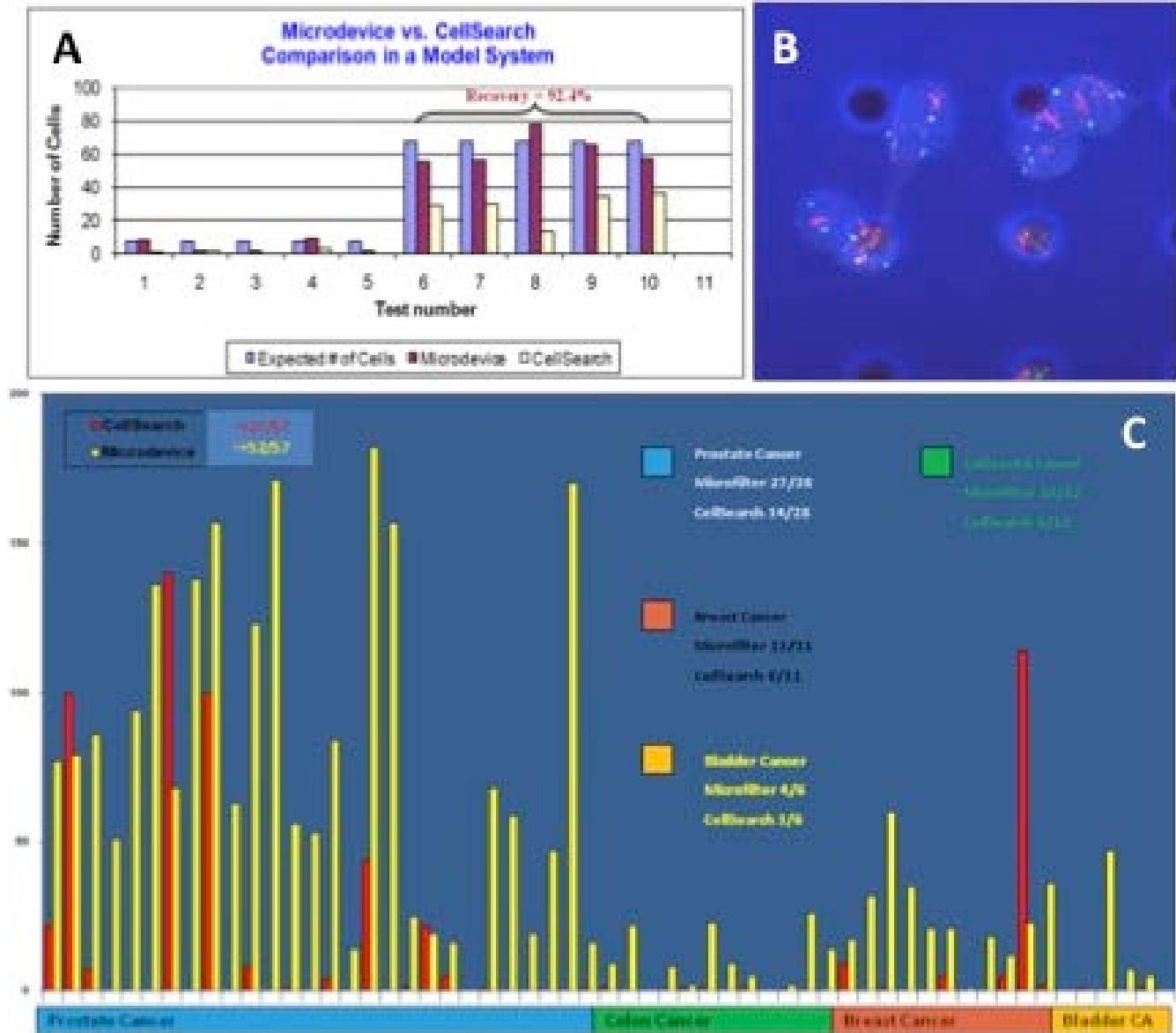
Key Research Accomplishments

- The microfilter device shows excellent yield with tumor cells seeded in 7.5 ml of blood captured with >90% efficiency, and a high throughput (7.5 ml of blood filtered in <5 minutes, 20 ml of blood in <10 minutes)
- CTC capture by the microfilter device favorably compares with commercially available technologies in corresponding blood samples (positive CTCs detected in 52/57 samples vs. 27/57 samples for the CellSearch platform)
- Dr. Yang's group successfully developed a prototype WFOV imaging platform to determine the resolution requirements necessary for CTC imaging on the microfilter device
- We have successfully developed the ability to acquire high-resolution, color images of tumor and no-tumor cells in model systems on the membrane microfilter device using a double-staining IHC protocol optimized in our laboratory to identify CTCs and non-tumor blood cells
- Although not in the proposed studies, analysis of CTCs in clinical blood samples using the WFOV scanning microscope is currently underway.

Progress

The microfilter device shows excellent yield with tumor cells seeded in 7.5 ml of blood captured with >90% efficiency (Figure 1A), and high-throughput capability (7.5 ml of blood filtered in <5 minutes, 20 ml of blood in <10 minutes) [4]. To test the device sensitivity, we performed 58 replicate experiments where five (5) tumor cells were seeded into 7.5ml donor blood. Based on these experiments, we determined that there is greater than 95% probability that when 5 tumor cells are present, the microfilter device will capture at least one cell [4]. This technology for CTC capture is shown to be substantially superior to commercially available FDA-approved immunomagnetic separation in blood from patients with cancer ([4]; Figure 1C).

Figure 1.

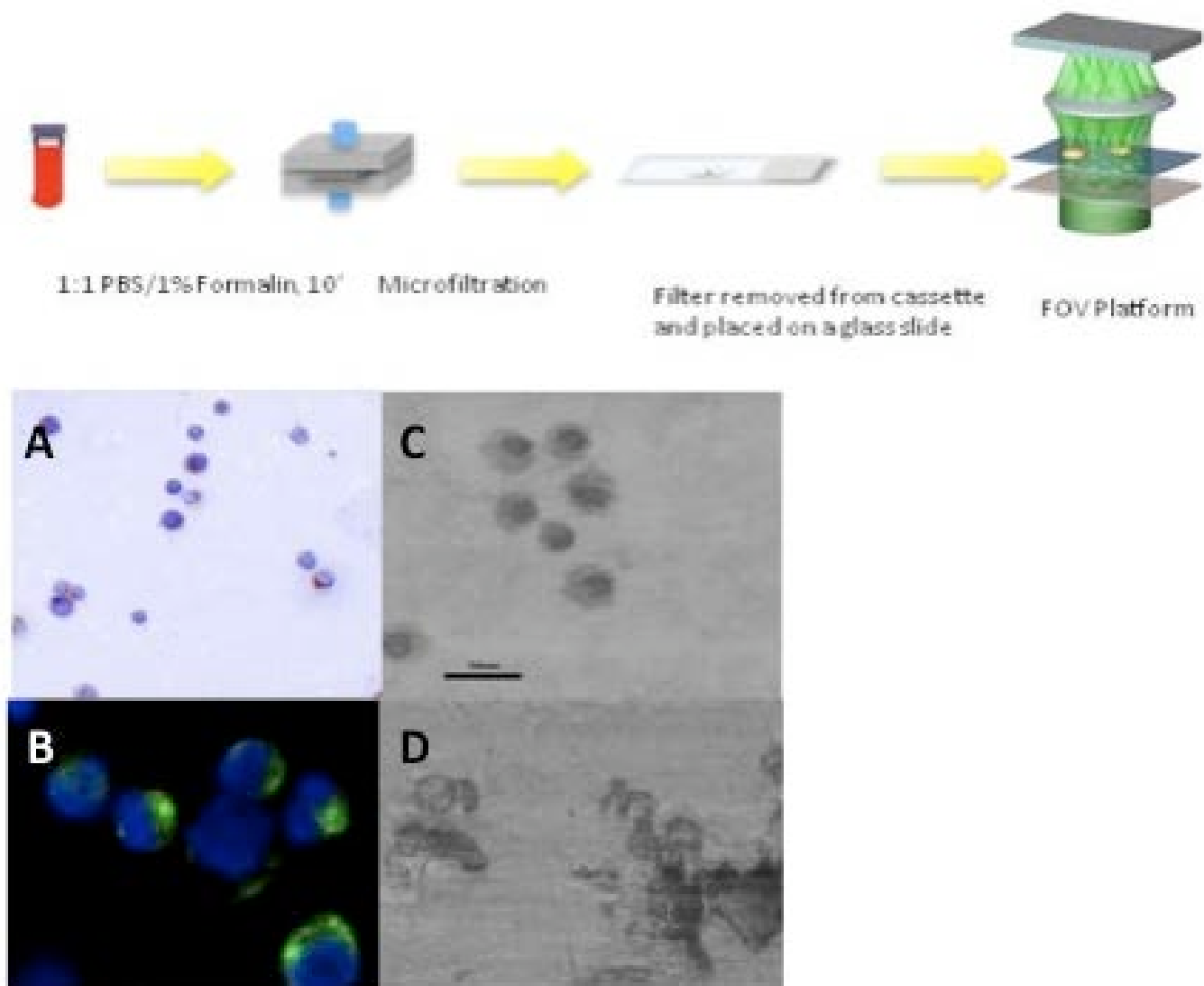


Additionally, using the SKBR-3 breast cancer cells captured by the microfilter device in a model system, we successfully performed fluorescent in-situ hybridization probing for Her2/Neu amplification, demonstrating an ability to perform molecular characterization on CTCs identified in breast cancer (figure 1B). **We have thus completed the task pertaining to Aim 1 of the proposed studies of achieving tumor cell capture through parylene-based microfiltration technology for breast cancer.**

Simultaneously, in association with our collaborator Dr. Yang (Caltech), we successfully demonstrated holographic scanning microscopy technique, which is highly stable and easy to scale (Aims 2 and 3). To achieve these Aims, 4 slides were prepared with cultured T24 Bladder Cancer Cells and processed as follows: 1) Stained for Cytokeratin (CK) using chromogenic staining with DAB 2) Stained for CK conjugated with Alexa 488 and DAPI, and 3) Negative Control Staining (slide incubated with no primary antibody but with only the

secondary antibodies), and 4) Unstained slide. All cell preparations were acetone fixed. The slides were sent at room temperature, and stained slides were cover-slipped. Each slide had low, medium and high cell density spots to help visualization by holographic scanning microscope (Figure 2 Schema). All slides were visualized and photographed at University of Miami before being sent, these records were compared with the images using holographic scanning microscope sent subsequently by Dr. Yang. The figures below show representative comparative images of chromogenically stained and fluorescently labeled T24 bladder cancer cells observed in brightfield (Figure 2A) and fluorescent (Figure 2B) microscopes, and the corresponding WFOV image. The WFOV system was able to successfully produced black and white images that allowed identification of subcellular compartments (i.e. nucleus and cytoplasm, Figure 2C, 2D). Based on these results we determined that, while potentially successful, the integration of an ideal imaging system for sensitive and rapid CTC analysis with the current microfilter device would require a platform capable of producing high resolution color images to distinguish chromagenic and/or fluorescent staining characteristics between tumor cells and non-tumor blood cells. Additionally, from these preliminary studies, our laboratories determined that sufficient CTC image analysis requires 0.6 μm resolution or better.

Figure 2.



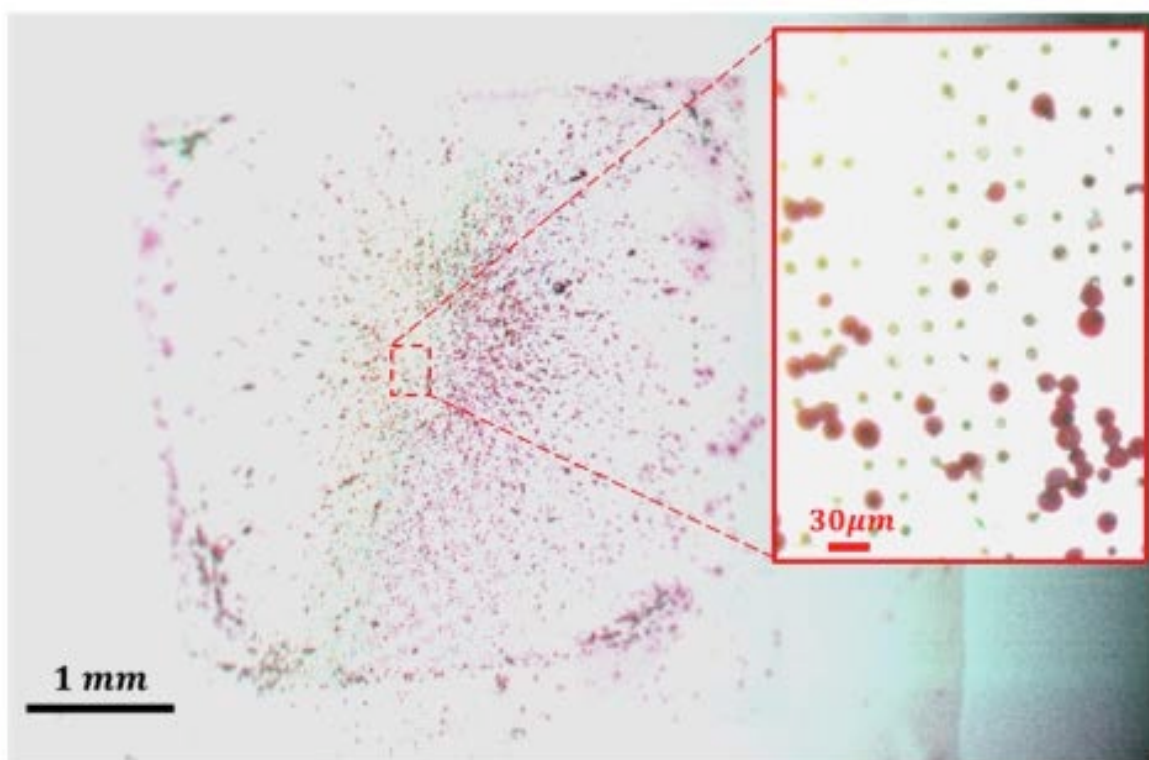
In 2011, we successfully evaluated an improved method based on the use of a Talbot grid in place of the hologram. This method simplifies the imaging scheme by using the Talbot self-imaging phenomenon to render a grid of highly focused light spots for scanning [3]. In 2012, we further evaluated the feasibility of using a flatbed scanner based microscopy imaging approach. This wide FOV microscopy imaging system uses a low-cost scanner and a closed-circuit-television (CCTV) lens. We showed that such an imaging system is capable

to capture a 10 mm * 7.5 mm FOV image with sub-micron resolution, resulting in 0.54 giga-pixels (109 pixels) across the entire image (26400 pixels * 20400 pixels). As a highly cost-effective scheme, this method became our prime candidate imaging method.

Thus, with the identification of imaging needs and parameters for CTC analysis using the microfilter device, and the initial development and evaluation of various novel WFOV methods in response to the established parameters, we successfully completed aims 2 and 3.

Using the parameters optimized in Aims 1, 2, and 3, we set out to collect high-resolution microscopic images of tumor cells captured by the microfilter device using a flatbed scanner based WFOV microscope system. Currently, cellular visualization by fluorescent imaging is unavailable. However, our lab developed a chromogenic double-staining IHC protocol for cell labeling that can be visualized at visible wavelengths (400-700nm). Briefly, rabbit polyclonal anti-human Pan Cytokeratin (CK) conjugated with a goat anti-rabbit secondary antibody containing alkaline phosphatase (AP) and mouse monoclonal anti-human CD45 conjugated with a goat anti-mouse secondary antibody containing horseradish peroxidase (HRP) were simultaneously used to label tumor cells and non-tumor nucleated blood cells, respectively. AP is reactive with Fast Red chromogen and HRP is reactive with diaminobenzidine (DAB), which produce two distinct colors visible by brightfield microscopy. Using a model system where MCF-7 cultured breast cancer cells (representing CTCs) and RAJI cultured lymphoma cells (representing non-tumor white blood cells) were mixed together and processed using the microfilter device. The double-staining IHC protocol described above was then used to label tumor and non-tumor cells captured by the microfilter device, and the high resolution holographic imaging system collaboratively developed by our groups was used to identify CK+/CD45- tumor cells. Scans using blue, green and red transmitted light are individually collected, and then recombined to generate a single color image. As demonstrated in figure 3, tumor and non-tumor blood cells with distinct morphologic features can be readily identified on the microfilter using our holographic imaging system. While not among the stated aims in this proposal, we have also undertaken analysis of CTC from actual patient samples as a natural extension of the proposed studies, and these analyses are underway. Thus far, we have processed three (3) blood samples drawn from patients with metastatic prostate cancer for imaging using the WFOV microscope system. **Based on our recent results, we report that Aim 4 has been successfully completed.**

Figure 3.



Reportable Outcomes

- Our CTC microfilter applicability in cancer patient samples has been documented in a publication in Clinical Cancer Research [4]. Our collaborators have published additional papers documenting the efficacy of the WFOV microscope and technology [3,5,6].
- We presented our data at the DoD Era of Hope conference in Orlando [1,2] (and are preparing a manuscript for publication specific to the collaborative study in the coming months.
- Based on this work, a proposal for the DOD Idea Expansion Award was submitted and funding support was successfully procured (W81XWH-11-BCRP-IDEX “Development of Laser-Mediated Nanodroplet Real-Time PCR on Circulating Tumor Cells Captured By Microfilter Platform”)
- No patents or licenses have yet resulted at University of Miami from this work, although our Caltech collaborator has filed for a number of patents.

Conclusion

In our work collaborative work to date, we have successfully completed studies for all four (4) specific aims set forth in this proposal.

References

Conference Abstracts

- 1). Datar R, Williams A, Wu J, Yang C, Cote R. Wide-field-of-view microscopy for breast cancer diagnosis. Poster Session P35, Detection and Diagnosis, Congressionally Directed Medical Research Programs. Era of Hope Meeting, Aug 2-5, 2011, Orlando World Center Marriott.
- 2). Yang C, Wu J, Cui X, Zheng G, Wang YM, Lee LM. Wide-field-of-view microscopy for breast cancer diagnosis. Poster Session P35, Detection and Diagnosis, Congressionally Directed Medical Research Programs. Era of Hope Meeting, Aug 2-5, 2011, Orlando World Center Marriott.

Publications

- 3). Wu J, Zheng G, Zheng L, Yang C. Focal plane tuning in wide-field-of-view microscopy with Talbot pattern illumination. Opt Letters. 2011; 36(12), 2179-2181.
- 4). Lin H, Zheng S, Williams A, Balic M, Groshen S, Scher HI, et al. Portable filter-based microdevice for detection and characterization of circulating tumor cells. Clin Cancer Res. 2010; 16, 5011-5018.
- 5). Wu J, Lee LM, Yang C. Focus grid generation by in-line holography. Opt Expr. 2010; 18(14), 14366-14374.
- 6). Wu J, Cui X, Zheng G, Wang YM, Lee LM, Yang C. Wide field-of-view microscope base on holographic focus grid illumination. Opt Letters. 2010; 35(13), 2188-2190.

List of personnel at University of Miami receiving pay from the research effort

Richard Cote
Ram Datar
Jorge Torres-Munoz
Siddarth Rawal

Poster P35-33

BC083697-3773

WIDE FIELD-OF-VIEW MICROSCOPY FOR BREAST CANCER DIAGNOSIS

Ram Datar², Anthony Williams², Jigang Wu¹, Changhui Yang¹, and Richard J. Cote²
 California Institute of Technology¹ and University of Miami School of Medicine²

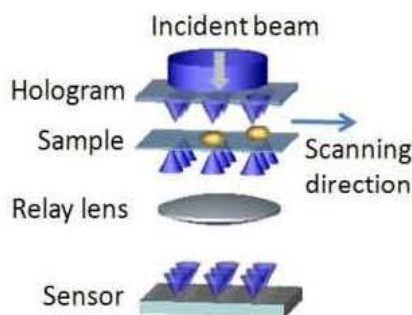


Fig. 1. WFM scheme

WFM Scheme

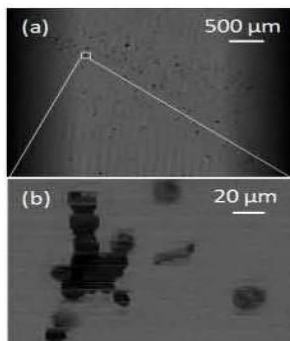


Fig. 2. Image of MCF-7 cells

Image of MCF-7 Cells

We have developed a novel microscopy technique that can acquire wide field-of-view images with resolution comparable to conventional microscopes. Our goal is to develop a cost-effective and high-throughput circulating tumor cell (CTC) analysis system applicable in cancer prognosis, therapeutic response monitoring, and target development.

The basic idea of the wide field-of-view microscopy (WFM) is to illuminate the sample by using a 2-D focus grid and measuring the transmission of the foci through the sample. The scheme is shown in Figure 1. A hologram is used to transform the incident collimated beam into a 2-D focus grid. By translating the sample across the focus grid, we can acquire an image by detecting transmissions using a relay lens and an imaging sensor. It can be treated as a parallel scanning microscope. By using a large-area focus grid and a long translation distance of the sample, we can acquire a very wide field-of-view image. The

resolution is limited by the focal spot size because the spot size can be made very small, there is potential to increase resolution.

As a part of initial modeling studies, we provided Dr. Yang's laboratory with Cytospin preparations of MCF7 breast cancer cells stained by hematoxylin alone, eosin alone, and hematoxylin-eosin. Figure 2 shows an example wide field-of-view image of breast cancer cells MCF-7. Figure 2(a) shows the wide field-of-view image, which is 5.8 mm x 4.3 mm and Figure 2(b) shows the expanded view of the region as indicated in Figure 1(a). The images indicate that we can achieve a wide field-of-view and still can see the details of the cell as if using a conventional microscope.

Our ongoing studies include analyzing Cytospin preparations of MCF7 cells stained for immunofluorescence reagents including quantum dot (QD)-labeled secondary antibodies. The QDs used include QD585, QD605, QD625, and QD655. The goal of these second set of experiments will be to assess the ability of the WFM microscope to detect signals at different defined emission wavelengths. Once this ability has been demonstrated, we will attempt to (1) detect cells captured by our novel membrane microfilter technology by using hematoxylin-eosin staining and immunofluorescence and (2) detect multiple signals from cells captured by our novel membrane microfilter technology by using multimarker immunofluorescence.

This work was supported by the U.S. Army Medical Research and Materiel Command under W81XWH-09-1-0050.

0.54 giga-pixel wide-field-of-view microscopy using a flatbed scanner

Guoan Zheng,* Xiaoze Ou, and Changhui Yang

Department of Electrical Engineering, California Institute of Technology, Pasadena, CA 91125, USA

*gazheng@caltech.edu

Abstract: Microscopy imaging systems with very wide field-of-view (FOV) are highly sought in biomedical applications. In this paper, we report a wide FOV microscopy imaging system that uses a low-cost scanner and a closed-circuit-television (CCTV) lens. We show that such an imaging system is capable to capture a 10 mm * 7.5 mm FOV image with sub-micron resolution, resulting in 0.54 giga-pixels (10^9 pixels) across the entire image (26400 pixels * 20400 pixels). The resolution and aberration of the proposed system were characterized by imaging a USAF resolution target and a hole-array target. Microscopy image of a pathology slide was acquired by using such a system for application demonstration.

©2013 Optical Society of America

OCIS codes: (170.0110) Imaging systems; (170.4730) Optical pathology; (170.0180) Microscopy

References and links

1. A. VanderLugt, Optical signal processing (Wiley New York, 1992).
2. J. Gilbertson, J. Ho, L. Anthony, D. Jukic, Y. Yagi, and A. Parwani, "Primary histologic diagnosis using automated whole slide imaging: a validation study," BMC clinical pathology 6, 4 (2006).
3. <http://www.dmetrix.net/techtutorial1.shtml>.
4. G. Zheng, S. A. Lee, Y. Antebi, M. B. Elowitz, and C. Yang, "The ePetri dish, an on-chip cell imaging platform based on subpixel perspective sweeping microscopy (SPSM)," Proceedings of the National Academy of Sciences 108, 16889-16894 (2011).
5. W. Bishara, T. Su, A. Coskun, and A. Ozcan, "Lensfree on-chip microscopy over a wide field-of-view using pixel super-resolution," Optics Express 18, 11181-11191 (2010).
6. J. Wu, X. Cui, G. Zheng, Y. M. Wang, L. M. Lee, and C. Yang, "Wide field-of-view microscope based on holographic focus grid illumination," Optics letters 35, 2188-2190 (2010).
7. J. Wu, G. Zheng, Z. Li, and C. Yang, "Focal plane tuning in wide-field-of-view microscope with Talbot pattern illumination," Optics letters 36, 2179-2181 (2011).
8. J. Di, J. Zhao, H. Jiang, P. Zhang, Q. Fan, and W. Sun, "High resolution digital holographic microscopy with a wide field of view based on a synthetic aperture technique and use of linear CCD scanning," Applied optics 47, 5654-5659 (2008).
9. M. Lee, O. Yaglidere, and A. Ozcan, "Field-portable reflection and transmission microscopy based on lensless holography," Biomedical Optics Express 2, 2721-2730 (2011).
10. K. Fife, A. Gamal, and H. Wong, "A 3mpixel multi-aperture image sensor with 0.7 um pixels in 0.11 um cmos," in IEEE ISSCC Digest of Technical Papers, (2008), 48-49.
11. M. Ben-Ezra, "Large-Format Tile-Scan Camera," IEEE Computer Graphics and Applications, 49-61 (2011).
12. S. Wang and W. Heidrich, "The Design of an Inexpensive Very High Resolution Scan Camera System," Computer Graphics Forum 23, 441-450 (2004).
13. S. A. Lee, R. Leitao, G. Zheng, S. Yang, A. Rodriguez, and C. Yang, "Color Capable Sub-Pixel Resolving Optofluidic Microscope and Its Application to Blood Cell Imaging for Malaria Diagnosis," PloS one 6, e26127 (2011).
14. J. Mallon and P. F. Whelan, "Calibration and removal of lateral chromatic aberration in images," Pattern recognition letters 28, 125-135 (2007).
15. http://www.linhofstudio.com/products/cameras/anagramm_digital_reproduction/anagramm_digital_reproduction.html.
16. G. Zheng, C. Kolner, and C. Yang, "Microscopy refocusing and dark-field imaging by using a simple LED array," Optics letters 36, 3987-3989 (2011).

1. Introduction

The conventional microscope architecture can be generally defined as consisting of a microscope objective for light collection from a sample slide, intermediate relay optics and a pair of or a singular eyepiece that projects a magnified image of the sample into our eyes. With the advancement of digital cameras, the eyepiece(s) segment of the microscope has undergone adaptation changes to be replaced with appropriate optics and camera to enable electronic imaging. Over the past decades and with the broad acceptance of infinity correction, the conventional microscope design has achieved extensive standardization across the microscopy industry - objectives and eyepieces from the major microscope makers are largely interchangeable. This standardization helps with cost-effectiveness. However, it has also limited the commercial design space for conventional microscopy - any significant design deviation that exceeds the standardization parameter space would have to contend with its incompatibility with the entrenched microscopy consumer base.

Recently, there has been an increased recognition that bioscience and biomedical microscopy imaging needs are outstripping the capability of the standard microscope. One salient need of modern bioscience and biomedical community is for a microscopy imaging method that is able to electronically acquire a wide field-of-view (FOV) image with high resolution. The standard microscope was originally designed to provide sufficient image details to a human eye or a digital camera sensor chip. As an example, the resolution of a conventional 20X objective lens (0.4 numerical aperture) is about $0.7\ \mu\text{m}$ and the FOV is only about 1 mm in diameter. The resulting space-bandwidth-product (SBP) [1] is about 8 mega-pixels (the number of independent pixels to characterize the captured image). This pixel count has only been recently reached or exceeded by digital camera imager. Interestingly, this SBP shows only slight variation across the range of commercial microscope objectives. Placed in different context, the relative invariance of SBP necessarily ties resolution and FOV together for most commercial objectives - high-resolution imaging necessarily implies a limited FOV.

In the past years, there has been significant progress in the development of system that increases the FOV of the conventional microscope system by incorporating sample slide scanning to acquire image over a large area [2] or by implementing parallel imaging with multiple objectives [3]. In addition, there have also been exciting research efforts into wide FOV imaging system, including ePetri dish [4], digital in-line holography [5], focus-grid scanning illumination [6, 7], off-axis holography microscopy [8, 9]. All these methods try to break the tie between resolution and FOV by abandoning the conventional microscopy design and shifting away from the use of optics schemes that perform optical image magnification.

The underlying assumptions that underpin all of these developments appear to be 1) a higher SBP (order of magnitude or more) with a magnification-based optical scheme is commercially impractical and 2) the associated pixel count for a radically higher SBP would face electronic image acquisition issues for which a viable solution does not yet exist.

In this paper, we demonstrate an optical magnification microscopy solution that challenges these assumptions. The configuration of this imaging system is based on two cost-effective items: a commercial available closed-circuit-television (CCTV) lens system and a low-cost consumer flatbed scanner. We show that, such a system is capable to capture a 0.54 giga-pixel microscopy image with a FOV of $10\ \text{mm} \times 7.5\ \text{mm}$ and that a sub-micron resolution is achieved across the entire FOV. Remarkably, the CCTV lens system has a SBP of at least 0.5 giga-pixel (10^9 pixels), which is about 2 orders of magnitude larger than those of conventional microscope objectives.

This paper is structured as follows: we will first present our proof-of-concept setup; then, we will present wide FOV images of a USAF target and a pathology slide that are acquired with our setup; next, we will characterize the aberration of the proposed imaging platform using a hole-array target; finally, we will discuss some limitations as well as future directions for the proposed giga-pixel microscopy system.

2. The prototype setup of the 0.54 giga-pixel microscopy imaging system

Driven by the recent trend of small pixel size of the image sensor ($0.7\mu\text{m}$ pixel size has been reported in Ref. [10]), significant efforts have been put into the design of consumer/industry camera lens to match this diffraction-limited pixel size. In the past years, it has been demonstrated that the SBP of some consumer camera lenses can achieve count on the order of billion pixels, i.e. these camera lenses are capable to capture giga-pixel images [11, 12].

In our proposed microscopy imaging system, we redirected this giga-pixel imaging effort [11, 12] to microscopy. The main component of the setup was a commercial available high-quality CCTV lens (C30823KP, Pentax, $f/1.4$, focal length 8mm). Like other consumer/industry camera lenses, the conventional use of this lens is to demagnify the scene onto the image plane, where the CMOS/CCD imager is located. In our setup (Fig. 1), we put our sample at the image plane to replace the CMOS/CCD imager and used the CCTV lens to magnify the sample, i.e. using the lens in the reverse manner. With a magnification factor of ~ 30 , the projected image was too large to be directly imaged with a CMOS/CCD imager. Instead, we modified and employed a consumer flatbed scanner (Canon LiDE 700F) to accomplish image acquisition. We chose this scanner for two reasons: 1) its “LED Indirect Expose (LiDE)” design and 2) the high scanning resolution (9600 dpi is claimed, corresponding to a $2.5\mu\text{m}$ pixel size). Due to its LiDE design, this scanner actually possesses a linear CCD that covers the complete width of the scanning area. In comparison, most other conventional scanners use a combination of mirrors and lenses to accomplish the same functionality.

In our setup, we disabled the LED light source of the scanner. The relay lens array and the light guide on top of the linear CCD were also removed. Therefore, the linear CCD shown in Fig. 1 was directly exposed to the projected image from the CCTV lens.

The scanning resolution was set to 2400 dpi (i.e. pixel size of scanner is $10\mu\text{m}$), and the FOV of the scanner was set to the maximum scanning area ($297\text{ mm} * 216\text{ mm}$), corresponding to a FOV of $10\text{ mm} * 7.5\text{ mm}$ on the object side. Based on these settings, the capture image contained 26400 pixels $*$ 20400 pixels, and thus, it produced a 0.54 giga-pixel microscopy image of the sample. Inset of Fig.1 shows the projected image of a USAF target on an A4 paper held in front of the scanner.

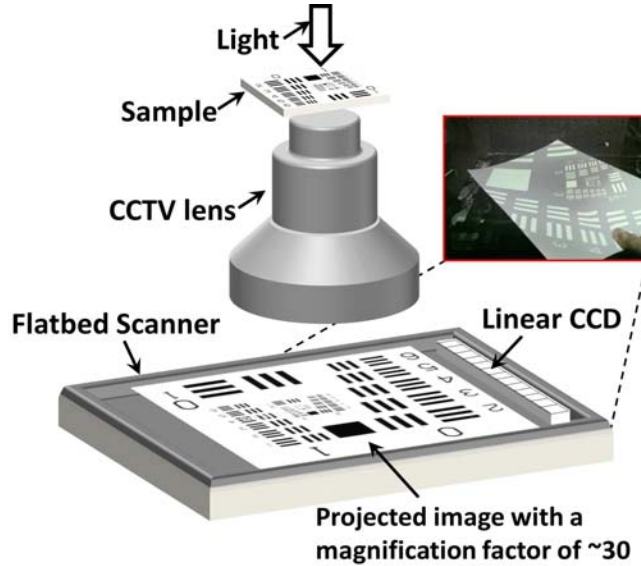


Fig. 1. The setup of the proposed 0.54 giga-pixel microscopy (not to scale). A CCTV lens is used to magnify the sample by a factor of 30 and a scanner is used to capture the projected image. The distance between the sample and the lens is about 1 cm. Inset on the top right shows the magnified image of a USAF target on an A4 paper held in front of the scanner.

3. Wide field-of-view imaging of a USAF target and a pathology slide

We next used our system for imaging demonstration. We first imaged a USAF target, as shown in Fig. 2. It is well known that, the aberration of a physical lens will degrade the image resolution at different FOVs of the lens, i.e. the resolution may be different from the center to the edge FOVs. In order to test the resolution at different FOVs, we translated the USAF target across the FOV of the CCTV lens and captured the corresponding images in Fig. 2(a-c). A white light source (white LED lamb, LIU004, Thorlabs) was used in this experiment to include the chromatic aberration in this resolution evaluation.

In the USAF target, the line widths of group 9, element 1, 2 and 3 are $0.98\ \mu\text{m}$, $0.87\ \mu\text{m}$ and $0.77\ \mu\text{m}$ respectively. The image performance at the center of the FOV is shown in Fig. 2(a), where we can clearly see the feature at group 9, element 3 ($0.77\ \mu\text{m}$ line width). In Fig. 2(b) and (c), we translate the sample to 50% and 95% of the FOV away from center (100% corresponds to 10 mm). In both images, we can still clearly see the fine feature at group 9, element 2 ($0.87\ \mu\text{m}$ line width). This establishes the resolution of our prototype system is $0.87\ \mu\text{m}$ over the entire FOV. However, we note that, in Fig. 2(c), the horizontal resolution is worse than the vertical resolution. Such an effect is due to the aberration characteristic of the lens and we will characterize this effect in the next section.

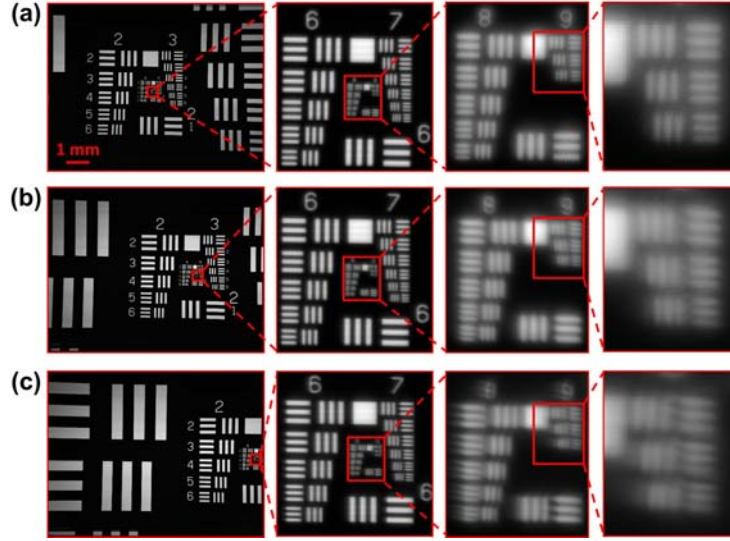


Fig. 2. USAF resolution target acquired by the proposed 0.54 giga-pixel microscopy system. The effective FOV is about $10\ \text{mm} \times 7.5\ \text{mm}$, with 26400 pixels \times 20400 pixels across the entire image. The imaging performance at the (a) center, (b) 50% away from center and (c) 95% away from center. The line widths of group 9, element 1, 2 and 3 are $0.98\ \mu\text{m}$, $0.87\ \mu\text{m}$ and $0.77\ \mu\text{m}$ respectively.

We also note that, due to slight pixel-response differences of the linear CCD, line-artifact is present in the raw scanning data [12]. This effect can be eliminated by performing a simple normalization process: 1) capture a reference image without any sample; 2) normalized the raw scanning image of the sample with the reference image. In this process, the reference image is sample-independent, i.e., it can be used for any sample.

For application demonstration, we acquired an image of a pathology slide in Fig. 3 (human metastatic carcinoma to liver, Carolina Biological Supply). We used R/G/B LED light sources for three color illuminations, similar to Ref. [13]. The sample slide was manually tuned to its in-focus position using a mechanical stage. The individual scan for focusing (only a small region of the scanner is used) took about 10-15 seconds. Three images (for R/G/B) are separately acquired, normalized, aligned [14] and then combined into the final color image. The scanner and magnification setting is the same as before. Fig. 3(a) shows the wide FOV image of the pathology sample. The FOV is about $10\ \text{mm} \times 7.5\ \text{mm}$, with 26400 pixels \times

20400 pixels. Fig.3 (b1), (b2) and (c1), (c2) are the corresponding expanded view for Fig. 3(a). We can see that our microscopy system can render a wide FOV microscopy image with fairly good resolution.

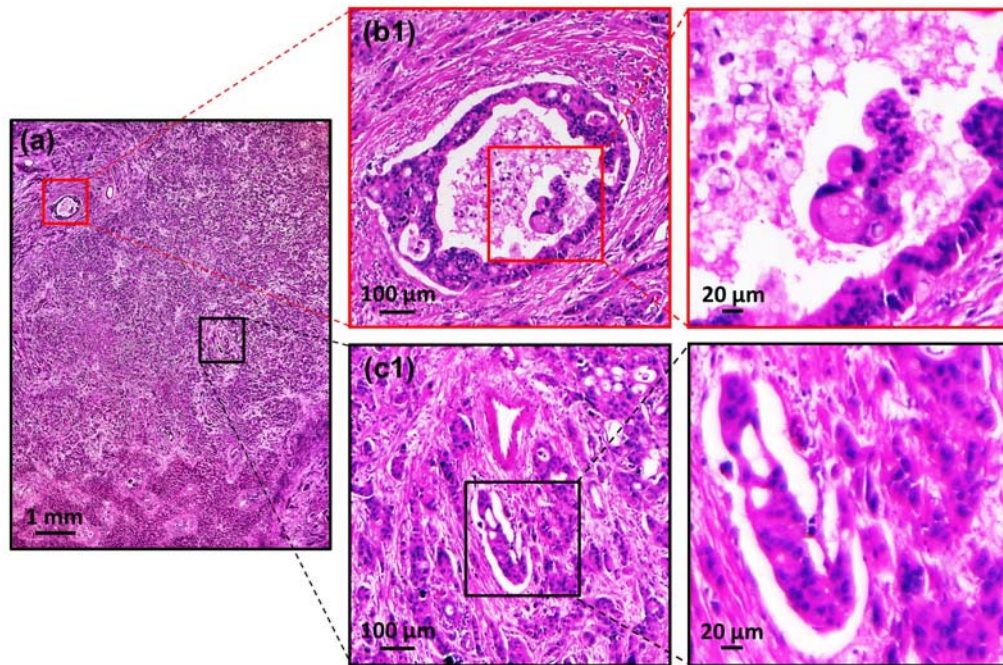


Fig. 3 Giga-pixel image of a pathology slide (human metastatic carcinoma to liver). The size of the image is 26400 pixels * 20400 pixels, and the FOV is about 10 mm * 7.5mm. (a) The full frame of the captured image. (b1), (b2) and (c1), (c2) are the expanded view of the (a).

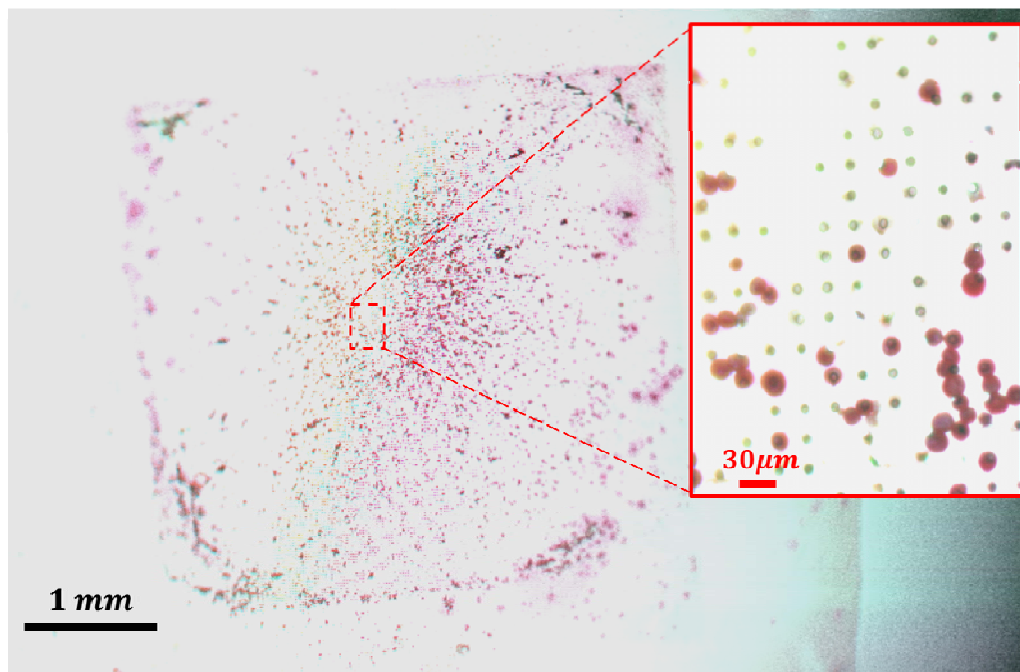


Fig. 4 Color image of the MFCD which contains CTCs (immunohistochemistry stained) collected by the large FOV microscopy system. The inset shows an expanded view of the region indicated by the dashed rectangle.

4. Aberration characterization across the entire field of view

Compared to the conventional microscope objective, one important limitation of the proposed system is the lens aberration. The design of the CCTV lens (or other consumer/industry camera lenses) has not been optimized for critical aberration correction as the microscope objective has. Due to the aberration, we can see the resolution degradation at edge of the FOV in Fig. 2(c). In this section, two experiments were performed to further characterize the aberration of the imaging system across the entire FOV. In both experiments, our sample was a chrome mask (1.8 cm * 1.8 cm) with a hole-array on it (fabricated by lithography). The size of the hole was about 1 μm in diameter and periodicity of the hole-array was 30 μm . The light source was the white LED lamp, the same as the source used in acquiring the image displayed in Fig. 2.

As we showed in Fig. 2(c), the resolutions in x and y directions are not the same if the area-of-interest is not at the center of the FOV. In the first experiment, we want to characterize this asymmetrical degradation effect across the whole FOV. The experiment was performed in the following steps: 1) we fine-tuned the z position of the chrome mask such that the captured image was in focus at the center FOV; 2) the whole image (with a 10 mm * 7.5 mm FOV) of the chrome mask sample was captured using the scanner; 3. we analyzed the full-width-at-half-maximum (FWHM) ratio of the captured spots across the whole FOV, both in the x and y directions (i.e. FWHM of spots at any FOVs normalized by the FWHM of spot at the central FOV). This ratio characterizes the aberration across the FOV of system. For example, a FWHM ratio of 2 means that the FWHM of a given spot is twice large as that of the central FOV. The result of this FWHM ratio is shown in Fig. 4(5), and we can see that: 1) the aberration becomes worse as the area-of-interest moves away from the central FOV; 2) FWHM ratio in x direction deteriorates faster than that in y direction, which is in good agreement of Fig. 2(c).

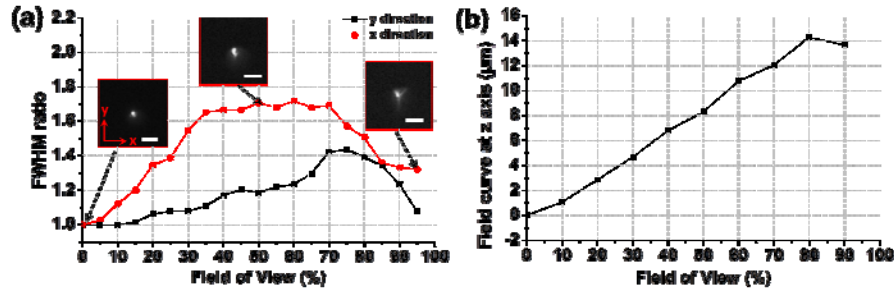


Fig. 5 (a) FWHM ratio of the spot size on different FOVs of the captured image. Left inset: the captured spot at the center FOV; middle inset: the captured spot at FOV 50% away from the center; Right inset: the spot at FOV 95% away from the center. Scale bar: 5 μm . (b) Displacement of the best focal plane of different FOVs (from center to edge FOV). In this figure, 100% in x-axis corresponds to 10 mm.

In the second experiment, we want to characterize the field curve of the imaging system. First, we captured a series of images as we mechanically shifted the chrome mask into different z positions; then, we analyzed the spot size to locate the best focal plane for different FOVs, with the result shown in Fig. 4(5). The displacement of best focal plane is directly

related to field curve of the imaging system. Remarkably, the result shows that the field curvature is relatively small (maximum observed of 14 micron z-displacement) over the entire FOV.

5. Conclusion

In summary, we report a wide-FOV (10 mm * 7.5 mm) microscopy system which can generate a 0.54 giga-pixel microscopy image with 0.87 μm resolution across the entire FOV. The CCTV lens in our platform is designed for 2/3 inch imager, and thus, the FOV limit is about 17 mm in diameter. However, the optical aberration becomes worse at the edge and sub-micron resolution cannot be claimed for a maximum FOV of 17 mm. We also note that there are other large-format professional camera lenses for even larger FOV (for example, 35 mm in diameter). Interested readers can choose their lenses based on the balance between the price and the performance.

It is interesting to contrast the SBP and resolution of our demonstrated system versus those of the conventional microscope. As shown in Fig. 6, the effective SBP of our system is more than one order of magnitude greater than those of the microscope objectives. Compared to a typical 10X and 4X objectives, our system has both superior SBP and resolution. Our current work did not include an exhaustive evaluation of all available commercial lens systems; driven by the power of consumer market, it is well possible that a lens system with even better SBP and/or resolution is commercially available.

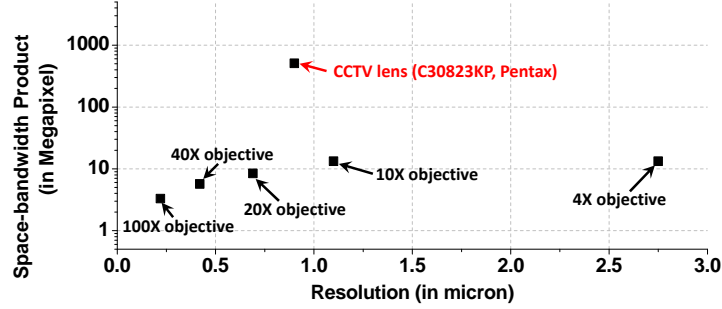


Fig. 6 The SBP-resolution summary for microscope objectives and the proposed system.

We note that one important limitation of the system is the scanning speed. The individual scans for focusing (only a small region of the scanner is used) took about 10-15 seconds each, while a full-scan at 2400 dpi scanning resolution with USB 2.0 link took about 10 minutes. There are three strategies to address this issue: 1) use other high speed scanners; 2) use multiple scanners for parallelization (we can take out the linear CCDs and its housing components from multiple scanners and assemble them into one scanner); 3) use other scanning devices such as the digital scanning back (for example, a commercial available digital scanning back takes 29 seconds to capture a 0.312 giga-pixel image [15]).

Our future directions include: 1) improve the speed of setup using the strategies discussed above; 2) incorporate other imaging functionalities such as 3D, darkfield and phase imaging into the proposed wide FOV platform [16, 17]; and 3) develop a fluorescence-capable giga-pixel microscopy platform.

Acknowledgements

We are grateful for the constructive discussions and generous help from Mr. Roarke Horstmeyer, Dr. Jigang Wu, Dr. Benjamin Judkewitz and Mr. Zheng Li from Caltech. We acknowledge funding support from the United States Department of Defense under grant W81XWH-09-1-0051.

Focal plane tuning in wide-field-of-view microscope with Talbot pattern illumination

Jigang Wu,^{1,2,*} Guoan Zheng,¹ Zheng Li,¹ and Changhui Yang^{1,3}

¹Department of Electrical Engineering, California Institute of Technology, 1200 East California Boulevard, Pasadena, California 91125, USA

²University of Michigan–Shanghai Jiao Tong University Joint Institute, Shanghai Jiao Tong University, Shanghai 200240, China

³Department of Bioengineering, California Institute of Technology, 1200 East California Boulevard, Pasadena, California 91125, USA

*Corresponding author: jigang@caltech.edu

Received April 15, 2011; accepted May 1, 2011;
posted May 10, 2011 (Doc. ID 145985); published June 6, 2011

We have developed a focal plane tuning technique for use in focus-grid-based wide-field-of-view microscopy (WFM). In WFM, the incidence of a collimated beam on a mask with a two-dimensional grid of aperture produced the Talbot images of the aperture grid. The Talbot pattern functioned as a focus grid and was used to illuminate the sample. By scanning the sample across the focus grid and collecting the transmission, we can generate a microscopy image of the sample. By tuning the wavelength of the laser, we can tune the focal plane of the WFM and acquire images of different depth into the sample. Images of a green algae microscope slide were acquired at different focal planes for demonstration. © 2011 Optical Society of America

OCIS codes: 170.0110, 050.1970, 170.5810.

The ability to collect wide-field-of-view (FOV) microscopic images is highly desired in many applications, such as digital pathology [1] or high-throughput screening [2]. There are numerous recent efforts aimed at addressing this need [3,4]. Previously, we have developed a wide-FOV microscope based on holographic focus grid illumination [5]. In that system, the sample is illuminated with a holographically generated grid of focused light spots, and the transmission of the light spots through the sample is projected onto an imaging sensor by a simple collection optics arrangement. A wide-FOV image can then be acquired by scanning the sample across the focus grid. Unlike conventional microscopy or other multi-beam microscopy [6], the resolution and FOV of such a system are not cross-competing design constraints. Here, the resolution is fundamentally set by the light spot size, and the FOV is set by the size of the holographic grid. As long as the collected light spot transmissions are well separated on the imaging sensor (determined by the spot separation and the collection optics), such a system can perform high-resolution wide-FOV microscopy imaging effectively.

In this Letter we demonstrate an alternate microscope design where the focus grid is generated via the Talbot effect. Here, a mask with an aperture grid is illuminated with a collimated laser beam to produce the focus grid. A “self-image” of the aperture grid will be reproduced at integer increments of the Talbot distance [7]. This focus grid replacement has several advantages. First, the focus grid generation is more repeatable and robust because the mask can be readily fabricated by the microfabrication technique. Second, unlike the holographic method, there is no zero-order transmission of the incident beam in the Talbot effect. This will enhance the contrast of the foci on the sensor and thus the signal-to-noise ratio of the image. Third, the focused light spots are more uniform in their powers (spot-to-spot comparison). Finally, this approach allows us to accomplish z -axis scanning

(focal plane change) by simply tuning the light source wavelength.

This Letter is structured as follows. We will briefly summarize the principle of the Talbot effect and point out certain subtleties that we have to closely consider in adapting the phenomenon for our specific applications. Next, we will describe our experimental setup. We will then report on our demonstration of focal plane tuning and apply the system to perform imaging.

The Talbot effect [8] is a well-known phenomenon in which the transmission from a mask with a periodic grid of apertures will reproduce the grid pattern at regular distance intervals from the mask. The distance interval, termed the Talbot distance Z_T , can be calculated as

$$Z_T = 2d^2/\lambda, \quad (1)$$

where d is the period of the pattern and λ is the wavelength. The periodic pattern will reproduce itself at the distance $Z = mZ_T$ or a phase-reversed image at $Z = (m - 1/2)Z_T$, where m is an integer. In principle, any of these planes can be used as the focus grid for our wide-FOV microscope. In our experiment, we used the second phase-reversed Talbot plane ($Z_{1.5} = 1.5Z_T$) for more convenient experimental setup.

Interestingly, Eq. (1) implies that Z_T is inversely proportional to the wavelength. For small tuning of the wavelength, i.e., $\Delta\lambda \ll \lambda$, the Talbot distance change can be calculated as

$$\Delta Z_T = -2d^2\Delta\lambda/\lambda^2. \quad (2)$$

For a periodicity $d = 30\ \mu\text{m}$ and a nominal wavelength of 700 nm, this implies that we can accomplish a significant plane shift of $55\ \mu\text{m}$ at $Z = Z_{1.5}$ for a small wavelength change of 10 nm. This tuning ability can be used in our microscope design to accomplish the non-mechanical focal plane shift.

As the resolution of our microscopy system depends on the grid spot size generated, the spot size that can be created by the Talbot effect is of importance to us. It is worth noting that the “self-imaging” ability of the Talbot effect is only a paraxial approximation [9]. In other words, the Talbot effect will “self-image” the holes in the mask well only if the hole diameter is much larger than λ [10,11]. The effect will fail and result in “self-image” spots that are substantially larger if the hole diameter is comparable to λ .

As we desire tightly focused light spots for our microscopy application, a straight application of the Talbot effect would not work well. Fortunately, we found that the Talbot field propagation will create tight light spots in planes that are slightly above the Talbot planes. Figures 1(a) and 1(b) show numerical simulations versus experimental characterization of the evolving Talbot patterns around $Z = Z_{1.5, \lambda 1}$ for $\lambda_1 = 702 \text{ nm}$. Our Talbot mask has a periodicity of $30 \mu\text{m}$ and aperture sizes of 800 nm . Figure 1(a) is the simulation results, and Fig. 1(b) shows experimental spots observed under a conventional microscope with a $60\times$ objective. The simulation was performed by the angular spectrum propagation using Fourier transforms. The Z positions and w , the FWHM, of spots except those in the last column are indicated in the figure. The last column corresponds to $Z = Z_{1.5}$. As we can see, the Talbot effect fails to generate a good focal spot at this position (the self-imaging approximation is not valid for this regime).

We further experimentally imaged the spot pattern at wavelength of $\lambda_2 = 692 \text{ nm}$ [Fig. 1(c)]. It is worth noting that the patterns closely resemble the original set. This is not surprising as the wavelength shift is small. It is further worth noting that the entire pattern set has shifted by a distance of $55 \mu\text{m}$ ($Z = Z_{1.5, \lambda 2} - Z_{1.5, \lambda 1} = 55 \mu\text{m}$) away from the mask. This shift is consistent with the prediction from Eq. (2).

Figure 1 also shows that the light pattern generally consists of a bright central spot and associated concentric rings. As the Z position increases, the center spot gets brighter and larger, while the concentric rings get smaller and finally disappear. By observing the evolving spots, we can see that the best focus spots for imaging are those around $Z_{1.5} - 90 \mu\text{m}$. For smaller z positions, the center spot is too weak for a good contrast imaging. While for larger Z positions, the center spot is too large to provide high-resolution images. The observed spots

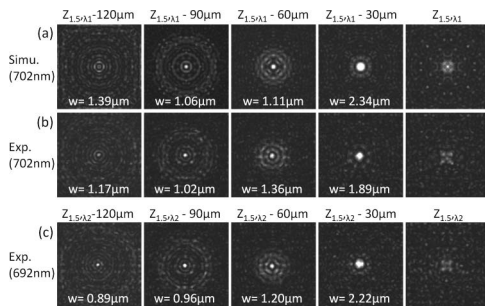


Fig. 1. Evolving of Talbot patterns around $Z = Z_{1.5}$. (a) Simulation spots for $\lambda_1 = 702 \text{ nm}$. (b) Spots for $\lambda_1 = 702 \text{ nm}$. (c) Spots for $\lambda_2 = 692 \text{ nm}$. w is the FWHM spot size, and $Z_{1.5, \lambda 2} - Z_{1.5, \lambda 1} = 55 \mu\text{m}$. The size of each pattern figure is $30 \mu\text{m} \times 30 \mu\text{m}$.

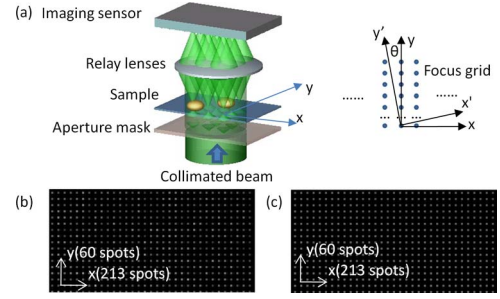


Fig. 2. (Color online) (a) Experimental setup of the wide-FOV microscope based on the Talbot illumination. (b) Part of the aperture grid on the mask plane. (c) Part of the focus grid at $Z = Z_{1.5}$. The number of spots along the x and y directions for the full mask is indicated.

show that we can get a resolution of $\sim 1 \mu\text{m}$, which was verified by acquiring images of a United States Air Force (USAF) target in the experiment.

Our experimental setup is shown in Fig. 2(a). An aperture mask was illuminated by a collimated beam introduced from a tunable Ti:sapphire laser (Spectra-Physics). As mentioned earlier, we employed an aperture mask with periodicity of $d = 30 \mu\text{m}$ and aperture size of 800 nm . The laser wavelength was tuned from 692 to 702 nm to vary the Talbot distance. The distance between the mask and the sample was set at $Z = Z_{1.5}$ during initial alignment. We subsequently fine-tuned the distance to make use of the tighter light spots discussed in the previous paragraph.

According to Eq. (2), the tuning range of the focal plane position was $55 \mu\text{m}$ in the experiment. Similar to the setup in our previous paper [3], the sample was illuminated by the focus grid and the transmission of the foci was projected by relay lenses (NT45-760, Edmund Optics, Inc.) onto an imaging sensor (LuCam080M, Lumenera Corp.). The sample was scanned across the focus grid and the scanning direction (y' direction) was slightly tilted at a small angle θ with respect to the focus grid, which was oriented at the x and y directions. The image can be reconstructed by combining line scans from each focal spots and properly shifting each line according to the scanning speed.

Figures 2(b) and 2(c) show part of the aperture grid on the mask plane and part of the focus grid at $Z = Z_{1.5}$, respectively. We can see that the intensity uniformity of the focus grid is better than the original aperture grid. The averaged relative adjacent spot intensity variation is 4% for the focus grid and 20% for the original aperture grid. This is reasonable, because many apertures will contribute to a focal spot; thus, the intensity difference of the original aperture grid will be partially averaged out. During image processing, we further ensure image uniformity by normalizing each scan line to compensate for the nonuniformity intensity distribution of the focal spots in the experiment.

We next used our system for imaging demonstration. The focus grid we used has 213×60 (in the x and y directions, respectively) spots, and the scanning was performed along the y' direction. Thus the reconstructed image is oriented at the x' and y' directions. The image will have a sawtooth shape at the starting and ending part because of the linear scanning characteristics.

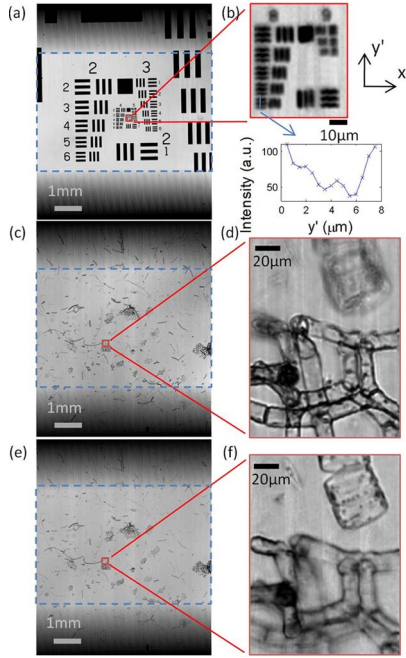


Fig. 3. (Color online) Images acquired by the Talbot wide-FOV microscope with an effective FOV of $6.4\text{ mm} \times 4.2\text{ mm}$. (a) Wide-FOV image of a USAF target, with effective FOV indicated in the large dashed rectangle. (b) Expanded view of the smallest feature of the target and cross-sectional profile of group 8, element 6. (c) Wide-FOV image of a mixed green algae slide with $\lambda = 692\text{ nm}$, with effective FOV indicated in the large dashed rectangle. (d) Expanded view of the region indicated in (c). (e) Wide-FOV image of a mixed green algae slide with $\lambda = 702\text{ nm}$, with effective FOV indicated in the large dashed rectangle. (f) Expanded view of the region indicated in (e).

The effective FOV in x' direction is $213^\circ d \approx 6.4\text{ mm}$. In the experiments, the sample was moved at a speed of $v = 0.165\text{ mm/s}$ for $L = 6\text{ mm}$. At the same time, the imaging sensor acquired 12,000 frames at $F = 330\text{ frames/s}$. The exposure time of the sensor was 0.5 ms . Thus, the sampling distance in the y' direction is $v/F = 0.5\text{ }\mu\text{m}$. The sampling distance in the x' direction is determined by the angle θ between the scanning direction (y' direction) and the grid orientation (y direction), which was set to be 0.0167 . Thus the sampling distance in x' direction is $d^* \sin(\theta) = 0.5\text{ }\mu\text{m}$. The effective FOV in the y' direction can be calculated by $L - H = 4.2\text{ mm}$, where $H = 60^\circ d = 1.8\text{ mm}$ is the extent of the focus grid in the y direction.

For the resolution test, we first image a USAF target, as shown in Figs. 3(a) and 3(b). Figure 3(a) is a wide-FOV image ($6.4\text{ mm} \times 4.2\text{ mm}$), and Fig. 3(b) is the expanded view of the region indicated in Fig. 3(a). The cross-sectional profile of group 8, element 6 is also shown in the figure. We can see that features sized with a line

width of $1.1\text{ }\mu\text{m}$ (group 8, element 6) can be resolved, which agrees with the measured spot size of $\sim 1\text{ }\mu\text{m}$ as shown in Fig. 1.

We then acquired images of a mixed green algae microscope slide (Carolina Biological Supply Company). Images were acquired at different focal planes, where Fig. 3(c) is for $\lambda = 692\text{ nm}$ and Fig. 3(e) is for $\lambda = 702\text{ nm}$. Figures 3(d) and 3(f) show the expanded view of corresponding regions indicated in Figs. 3(c) and 3(e), respectively. We can see that Figs. 3(d) and 3(f) were focusing at different focal planes and were able to render high-resolution images of the sample at different planes.

At this point, it is worth noting that it is unclear if this Talbot illumination approach can provide resolution better than $1\text{ }\mu\text{m}$. It may be possible to design the aperture geometry to diffract more light at large angles to help in tighter focus spot generation. The spot quality will also be degraded for thick scattering samples, especially when the focus spot is tighter.

In summary, we report a wide-FOV microscope based on Talbot pattern illumination. The wavelength of the laser source can be tuned to change the focal plane distance in order to obtain images at different focal planes. The elimination of mechanical scanning along the focal axis can be a significant advantage for fast scanning microscopy applications. The focal spot size was measured to be $\sim 1\text{ }\mu\text{m}$ under a conventional microscope. Images of a USAF target and a mixed green algae microscope slide with an FOV of $6.4\text{ mm} \times 4.2\text{ mm}$ are acquired for demonstration of the system.

This work is supported by the United States Department of Defense under grant W81XWH-09-1-0051. The authors acknowledge Richard Cote and Ram Datar from the University of Miami for helpful discussions.

References

1. J. Ho, A. V. Parwani, D. M. Jukic, Y. Yagi, L. Anthony, and J. R. Gilbertson, *Hum. Pathol.* **37**, 322 (2006).
2. M. Oheim, *Br. J. Pharmacol.* **152**, 1 (2007).
3. W. Bishara, T. W. Su, A. F. Coskun, and A. Ozcan, *Opt. Express* **18**, 11181 (2010).
4. M. G. Rojo, G. B. Garcia, C. P. Mateos, J. G. Garcia, and M. C. Vicente, *Int. J. Surg. Pathol.* **14**, 285 (2006).
5. J. Wu, X. Cui, G. Zheng, Y. M. Wang, L. M. Lee, and C. Yang, *Opt. Lett.* **35**, 2188 (2010).
6. R. Graf, J. Rietdorf, and T. Zimmermann, *Adv. Biochem. Eng. Biotechnol.* **95**, 1311 (2005).
7. J. R. Leger and G. J. Swanson, *Opt. Lett.* **15**, 288 (1990).
8. H. F. Talbot, *Philos. Mag.* **9**, 401 (1836).
9. K. Paturski, *Prog. Opt.* **27**, 1 (1989).
10. B. Besold and N. Lindlein, *Opt. Eng.* **36**, 1099 (1997).
11. E. di Mambro, R. Haidar, N. Guerinneau, and J. Primot, *J. Opt. Soc. Am. A* **21**, 2276 (2004).

Published in final edited form as:

Clin Cancer Res. 2010 October 15; 16(20): 5011–5018. doi:10.1158/1078-0432.CCR-10-1105.

APPENDIX 4

Portable Filter-Based Microdevice for Detection and Characterization of Circulating Tumor Cells

Henry K. Lin^{1,*}, Siyang Zheng^{2,*}, Anthony J. Williams³, Marija Balic⁴, Susan Groshen⁵, Howard I. Scher⁶, Martin Fleisher⁷, Walter Stadler⁸, Ram H. Datar³, Yu-Chong Tai⁹, and Richard J. Cote^{3,10}

¹Biosciences Division, Oak Ridge National Laboratory, Oak Ridge, TN 37831, USA

²Department of Bioengineering, The Pennsylvania State University, University Park, PA 16802, USA

³Department of Pathology, University of Miami Miller School of Medicine, Miami, FL 22136, USA

⁴Department of Oncology, Medical University of Graz, Graz, Austria

⁵Department of Preventive Medicine, University of Southern California Keck School of Medicine, Los Angeles, CA 90033, USA

⁶Genitourinary Oncology Service, Memorial Sloan-Kettering Cancer Center, New York, NY 10065, USA

⁷Department of Clinical Laboratories, Memorial Sloan-Kettering Cancer Center, New York, NY 10065, USA

⁸Department of Medicine, University of Chicago Pritzker School of Medicine, Chicago, IL 60637, USA

⁹Department of Electrical Engineering, California Institute of Technology, Pasadena, CA 91125, USA

Abstract

Purpose—Sensitive detection and characterization of circulating tumor cell (CTC) could revolutionize the approach to patients with early stage and metastatic cancer. The current methodologies have significant limitations including limited capture efficiency and ability to characterize captured cells. Here, we report the development of a novel parylene membrane filter-based portable microdevice for size-based isolation with high recovery rate and direct on-chip characterization of captured CTC from human peripheral blood.

Experimental Design—We evaluated the sensitivity and efficiency of CTC capture in a model system using blood samples from healthy donors spiked with tumor cell lines. 59 model system samples were tested for determining the recovery rate of the microdevice. Moreover, 10 model system samples and 57 blood samples from cancer patients were subjected to both membrane microfilter device and CellSearch® platform enumeration for direct comparison.

Copyright © 2010 American Association for Cancer Research

¹⁰To whom correspondence should be addressed. rcote@med.miami.edu, Address: 1611 N.W. 12th Avenue Miami, FL 33136 Phone: (305) 585-6103.

*Authors contributed equally

Author Contributions H.K.L., S.Z. and A. J. W. performed the experiments. All authors contributed to experimental design, data analysis and manuscript writing.

Competing interests statement: The authors declare no competing financial interests.

Results—Using the model system, the microdevice achieved >90% recovery with probability of 95% recovering at least one cell when 5 are seeded in 7.5 ml of blood. CTCs were identified in 51 out of 57 patients using the microdevice, compared to only 26 patients with the CellSearch® method. When CTC were detected by both methods, greater numbers were recovered by the microfilter device in all but 5 patients.

Conclusions—This filter-based microdevice is both a capture and analysis platform, capable of multiplexed imaging and genetic analysis. The microdevice presented here has the potential to enable routine CTC analysis in clinical setting for effective management of cancer patients.

The most important determinant of prognosis and management of cancer is the absence or presence of metastasis (1). The early spread of tumor cells to lymph nodes or bone marrow (BM) is referred to as “disseminated tumor cells” (DTC), or as CTC when observed in the peripheral blood. It has been well established that DTC or CTC can be present even in patients with no evidence of overt metastasis, and who have undergone complete resection of the primary tumor; this is the basis for the later development of overt metastases. Indeed, the possible presence of DTC or CTC is the rationale behind the use of systemic adjuvant chemotherapy in patients who have undergone definitive treatment of the primary tumor (2). Once there is clinical evidence of metastasis, patients will undergo systemic therapy. While the efficacy of such therapy is improving, many patients will not respond, even when appropriate targets have been identified (3). A growing body of evidence suggests that CTC monitoring can identify those patients that are responding to, or failing therapy early in the course of treatment, based on comparison of CTC counts before and after the initiation of treatment, allowing for earlier and more specific prediction of therapeutic efficacy (4-8). This application thus has the potential to fundamentally alter the way patients with metastatic cancer are managed.

The technical challenge for detection of CTCs is their extremely rare occurrence in blood, coupled with the task of correctly identifying tumor cells after enrichment. The number of CTCs in blood is rare in comparison to resident blood cells, which consists of white blood cells (WBCs) ($5-10 \times 10^6 \text{ ml}^{-1}$), red blood cells (RBCs) ($5-9 \times 10^9 \text{ ml}^{-1}$), and platelets ($2.5-4 \times 10^8 \text{ ml}^{-1}$). A variety of technologies for CTC isolation have been described (9), including methodologies exploiting the physical characteristics of tumor cells such as density (10), cell size (11,12), electrical properties (13), or expression of protein markers (14). Virtually all current systems depend on affinity based capture and enrichment, usually using antibodies to surface epithelial markers such as EpCAM (3). Affinity based systems are limited by the heterogeneity of expression of the target antigens, and also limited to the types of tumors expressing these antigens.

The current methodologies for CTC capture and identification in blood have significant barriers including multiple procedural steps, substantial human intervention, high cost, or most importantly, the lack of capture efficiency and standardization for the detection methods. Further, current methods have very limited ability to perform complex analysis of the captured cells, such as identification of targets or special biological characteristics (e.g. stem cell characteristics). Thus, there is a need for the development of a reliable, efficient platform to isolate, enrich and characterize CTC in blood. It would be highly desirable if such a capture device were portable and could be used at the point-of-care or in a reference laboratory to eliminate the variation in blood shipment conditions to centralized processing facility, enhancing clinical decision-making ability. This study describes development of such a clinical assay, explores its ability to capture more intact CTC than the FDA-approved CellSearch assay and presents data to show that it does so favorably. We believe this is a significant step forward towards analytical validation of a novel technology.

Patients and Methods

Cell Culture and Harvest

Carcinoma cell lines derived from different primary tumor sites were purchased from American Type Culture Collection (Manassas, VA) without further testing or authentication. All cell cultures were grown to confluence with the respective medium (RT4 and T24: McCoy's 5A, J82 and HT-1080: EMEM, LNCaP: RPMI, MCF-7, MDA-MB-231 and SK-BR-3: DMEM) supplemented with 50 units/mL of penicillin and streptomycin and 10% FCS (Mediatech, Inc., Herndon, VA) in a 75 cm² or 25 cm² tissue culture flask (Corning, Corning, NY) and maintained in a humidified incubator at 5% CO₂ and 37°C. Adherent cells were harvested using GIBCO® Trypsin-EDTA (Invitrogen Corp., Carlsbad, CA); we have demonstrated that expression of EpCAM is not affected by this process. Cell numbers were assessed using hemocytometer, and cell viability was measured using a dye exclusion method (Invitrogen Corp., Carlsbad, CA) where for each experiment, the cell viability showed at least 90% healthy cells after detachment from culture flask and washing steps.

Cell Size Measurement

To measure the diameter of cells in suspension, each of the cultured cell lines were suspended in PBS and loaded inside hemacytometers (Bright-Line, Hausser Scientific, Horsham, PA). Cells suspended over the etched grid were imaged using SPOT Insight Color camera (IN320, Diagnostic Instruments, Sterling Heights, MI). Each image was analyzed using MATLAB to obtain 4 coordinates manually to define the maximum diameter vertically and horizontally. Cell diameters were calculated by averaging the vertical and horizontal length. Measurements in pixels were converted into μm by utilizing the etched 50 μm grids within the hemocytometer as the reference scale bar.

Flow rate characteristics

To provide constant pressure source at the inlet of the microdevice, pressure regulators were connected in series from a CO₂ gas cylinder to a working range of 0-10 psi. A pressure meter (Omega pressure calibrator PCL 100-30, Stamford, CT, 30 psi maximum, 0.001 psi sensitivity) was connected near the inlet of microdevice for monitoring the pressure source. For each measurement, sample solution was first injected into an inlet reservoir with the valve to the 0.5 psi pressure source in the 'closed' position. Upon opening the valve to the pressure source, the time and flow rate were recorded where the flow rate was monitored through mass change in the outlet reservoir.

Recovery rates with model system

To measure the recovery rates of tumor cells in blood using the microdevice, a mixture of cultured tumor cells (MCF-7, SK-BR-3, J82, T24, RT4, LNCaP) were harvested and cell counts were obtained using a hemacytometer. Cells were serially diluted to the desired number per 10 microliters and the expected cell count was obtained by averaging 10 measurements using hemacytometer. For sensitivity studies, cell suspension droplets containing approximately 3,000 cells were placed on a microscope slide and the desired numbers of cells (10 or 5 cells) were manually aspirated. Cells were spiked in blood and diluted with PBS with final blood to buffer ratio of 1:1 containing 1% formalin. Each sample underwent partial fixation for 10 minutes with constant rotation. The sample was dispensed through the filter with a syringe and the filter containing captured cells was fixed in 10% NBF for 10 min followed by permeabilization of cell membrane with 0.25% triton X-100 (BioRad, Hercules, CA). Each filter was allowed to air-dry overnight at room temperature and subjected to immunofluorescence (IF) analysis to identify CTCs and distinguish them from the background of non-target blood cells.

On-Chip Immunofluorescence Detection of Captured CTC

Tumor cells were identified and distinguished from leukocytes based on morphology and differential antigen expression. Tumor cells are epithelial, and express cytokeratin (CK), while leukocytes are non-epithelial, and are negative for CK. IF was performed directly on the filter membranes for the expression of CKs. Filter membranes were placed on top of microscope slides and blocked with normal horse serum for 20 min. A cocktail of two different mouse monoclonal antibodies against CKs was used for the detection of epithelial tumor cells: AE-1 (1:600 dilution, Signet, Dedham, MA, cat. # 462-01) against low and intermediate Type I acidic keratins and CAM 5.2 (1:100 dilution, Beckton-Dickinson, San Jose, CA, cat. #349205) against CK 8 and 18. The slides were incubated for 1 hour in the cocktail of primary antibodies diluted in CheMate antibody diluent (DakoCytomation, Carpinteria, CA). Subsequently, the slides were washed and incubated for 1 hour with fluorescent, Alexa Fluor 488 conjugated goat anti-mouse secondary antibody (Invitrogen, Carlsbad, CA). For samples collected from patients with castration resistant prostate cancer, the entire procedure is repeated using rabbit polyclonal antibodies against PSA (Dako, Denmark, cat. # A0562) followed by Alexa Fluor 594 conjugated goat anti-rabbit secondary antibody (Invitrogen, Carlsbad, CA) to confirm that the CK positive cells were of prostate origin. Membrane on slides were coverslipped using Vectashield® (Vector Laboratories, Burlingame, CA) mounting medium containing 4',6-diamidino-2-phenylindole (DAPI) for nuclear staining and sealed with nail polish. IF images were obtained using Leica DM LB2 microscope equipped with Diagnostic Instruments 7.3.3 color camera viewed with Chroma filter sets consisting of excitation filters of 480/40 and 560/55, dichroic filters of 505 and 595 long pass, and emission filters of 535/50 and 560/55. Cells were imaged directly on filter membranes placed onto microscope slides.

Comparison of CellSearch® vs. Microdevice

Each blood sample collected in CellSave® preservative tube, provided by Quest Diagnostics, was spiked with mixture of cultured tumor cells (MCF-7, SK-BR-3, J82, T24, RT4, LNCaP) either by manual pipetting under microscopic visual control (10 cells) or serial dilution (90 cells). Although each sample collected in CellSave® tubes contains 10 ml of blood, the CellSearch® test only uses 7.5 ml of blood for their assay; therefore, in order to provide a direct comparison of performance, only 7.5 ml of blood was used in the analysis using the microdevice.

Patient Samples

Blood samples from patients with metastatic prostate, breast, colon or bladder cancer were obtained at Memorial Sloan-Kettering Cancer Center (MSKCC), New York, NY with appropriate informed consent from each patient. Each sample was collected using CellSave® tubes and shipped overnight in a styrofoam box at room temperature to our laboratory and processed immediately upon receipt. At the time of collection, a sample in CellSave tubes was also obtained and tested by the CellSearch® method at MSKCC.

Enrichment Count

To estimate the number of WBCs retained on the membrane, normal donor blood samples were processed through the filter, the cells were stained with DAPI and 30 images were captured using a fluorescence microscope with DAPI filter set. Each image was split into its red, green and blue component using the RGB split option with ImageJ, a free image processing software provided by NIH. The blue component was analyzed by using the automated particle analysis to detect circular objects within the field of view. Each nucleated cell was counted and averaged to provide an estimate to the number of WBC retained on each filter.

Results

We fabricated parylene membrane microfilters as described previously (15) and each device was constructed by sandwiching individual membrane filters with rectangular slabs of polydimethylsiloxane (PDMS) and clamped between acrylic jigs as shown in Figure 1 to form a fluidic chamber with openings from the top and bottom to create a sealed system with an inlet and an outlet.

One of the major requisites for the detection of CTC is the ability to preserve their morphology for cytopathological analysis, which is critical for the identification of true CTC. Fixatives stabilize the cells to protect them from the rigors of subsequent processing and staining techniques. The use of precipitation-based fixatives such as alcohol and acetone result in formation of large aggregates of serum protein, which can quickly clog filters resulting in device failure. Therefore, a formaldehyde-based fixative, which forms methylene cross-links between basic amino acids was used for preservation of morphology in this study. Because the extent of methylene bridges depends upon various factors including concentration of formaldehyde, temperature, pH and time of exposure, with over-fixation resulting in formation of large clumps leading to device failure, we optimized the fixation protocol for blood so as to preserve CTC morphology while allowing a desirable flow rate through the filter. Different fixative concentrations, between 0.1-10% neutral buffered formalin in PBS (NBF, VWR®) were tested for cultured tumor cells, and the fixation by 1% formalin was found to be optimal for preserving morphology while retaining desirable flow rate (data not shown). In addition, flow characteristics of different samples were monitored using a constant pressure source for sample delivery while the flow rate was indirectly monitored by measuring the weight of the flow-through liquid in relation to time. Flow rates under constant pressure (0.5 psi) of samples with different fixatives (acetone and formalin), concentrations of NBF (0%, 1%, and 5%), dilutions of blood (100% and 50%) and amount of cultured tumor cells (0, 25,000 and 50,000) were measured and plotted in Figure 2. The most important determinant of flow property is the composition of the fluidic components in the sample, including cellularity of blood and concentration of fixative. The optimized protocol was 10 minute rotational fixation of blood diluted in equal volume of buffer containing 2% formalin; the final dilution of blood was 50%, and final formalin concentration was 1%.

As a model system to optimize our device, we evaluated the sensitivity and efficiency of CTC capture using the membrane microfilter device. Five cultured human cancer cells were manually micro-pipetted with observation under microscope into 7.5 ml of whole blood from healthy, cancer-free donors, and processed by the membrane microfilter device. A total of 58 replicates were performed, where half of the replicates (29) were seeded with only J82 bladder cancer cell line, which is relatively small in size ($14 \pm 1.5 \mu\text{m}$), and the other half were seeded with a mixture of 6 different human cancer cell lines (J82 and T24 bladder cancer cell lines, MCF-7, SK-BR-3, and MDA-MB-231 breast cancer cell lines, and LNCaP prostate cancer cell line). The heterogeneity of tumor cells can be modeled using cells from a mixture of unsynchronized cell cultures with varying cell sizes as shown in Figure 3a. Cell sizes of cultured tumor cells ($14 \mu\text{m} \sim 19 \mu\text{m}$) are smaller compared to CTCs from breast cancer patients ($15 \mu\text{m} \sim 30 \mu\text{m}$) (16), making the model system more challenging for size-based enrichment. The membrane microfilter device successfully recovered 1+ tumor cell in 96.5% (28/29) and 93.1% (27/29) of trials when five cells from single J82 cell line and a mixture of 6 different human cancer cell lines were seeded into 7.5 ml blood from a healthy donor, respectively. Furthermore, the microfilter device recovered 3 or more cells in 64% of trials. Statistical analysis showed that true probability of recovering at least one cell when 5 are seeded in 7.5 ml of blood is 95% with the 95% confidence interval between 85% and 99%, which provides a sensitive assay to detect rare event. Due to optically transparent

nature of parylene filter, we were able to perform microscopic and IF analysis of cells “on-chip”, that is directly on the membrane, circumventing the need to transfer cells for analysis. Tumor cells were identified and distinguished from leukocytes by expression of CK antigens by IF; epithelial tumor cells are CK positive, while leukocytes are CK negative (Figure 3a). Moreover, CK positive CTCs captured from prostate cancer patients were imaged on membrane, showing both prostate specific antigen (PSA) positive (Figure 3b, c) and negative (Figure 3d) CTCs. We also examined negative control samples from 10 healthy individuals and none of the samples from healthy subjects had any detectable CTCs.

We also compared the performance of the microdevice for enumeration of tumor cells against a commercially available platform, the FDA-approved CellSearch® system, performed by Quest Diagnostics (San Juan Capistrano, CA) in a model system and at Memorial Sloan-Kettering Cancer Center (MSKCC), New York, NY in clinical samples. The initial set of samples using the model system were prepared in duplicates; one set was subjected to in-house microfilter-based CTC detection, while the replicate was sent for CellSearch® analysis. For the comparison of sensitivity, two sets of 5 replicates were prepared, where 10 cultured cancer cells were manually spiked under visual control into 10ml volumes of blood collected intravenously from healthy donors. Although 10ml of blood is collected, only 7.5 ml is actually tested using the CellSearch® assay per instruction from CellSearch® system. Therefore, we tested only 7.5 ml of collected blood in the microfilter device (final cell yield of 7 - 8 cells). One set of 5 replicates was shipped for CellSearch® analysis, while the other set of 5 replicates was subjected to microdevice analysis. The microdevice was able to detect at least 1 cell when 7 - 8 cells were spiked with all 5 replicates (mean = 4.6, median = 2) while the CellSearch® system detected at least 1 cell in only 3 replicates (mean = 1.2, median = 1). For the comparison of recovery rate, 5 more duplicates of blood collected from normal donor were spiked with 90 cultured cancer cells obtained through serial dilution; again, 1 set was sent for CellSearch® analysis, while the other was subjected to in house microdevice separation. The microfilter device vs. the CellSearch® system achieved recovery rates of $92 \pm 14\%$ vs. $42 \pm 13\%$, respectively, where the microfilter device significantly outperformed the CellSearch® system ($p = 0.0005$, t-test, $n=5$, performed at Quest Diagnostics Inc.).

To compare the performance of microfilter device vs. CellSearch® using patient samples, we collected and processed a total of 57 samples from patients with metastatic cancer: prostate ($n = 28$), breast ($n = 11$), colorectal ($n = 12$), and bladder ($n = 6$). CTCs were identified in 51 patients using the microdevice, compared to only 26 patients with the CellSearch® method as tabulated in Table 1. Each CTC capture operation is completed in less than 2 minutes. The number of CTCs isolated ranged from 0 to 182 vs. 0 to 140 (microdevice vs. CellSearch®) per sample for prostate cancer (96 ± 47 vs. 18 ± 39 , mean \pm SD), 1 to 60 vs. 0 to 114 for breast cancer (25 ± 15 vs. 12 ± 34), 0 to 26 vs. 0 to 1 for colorectal cancer (10 ± 9 vs. 0.3 ± 0.5) and 0 to 47 vs. 0 to 1 for bladder cancer (10 ± 18 vs. 0.3 ± 0.5). As shown in Figure 4, the microfilter device outperformed the CellSearch® system in terms of recovery rates for all cancer types. When CTC were detected by both methods, greater numbers were recovered by the microfilter device in all but 5 patients. Immunomagnetic bead-based and carbon micropost enrichment methods depend on the expression of a specific surface antigen, EpCAM on the target tumor cells. EpCAM is expressed by only 75% of 134 epithelial tumors (17). In contrast, the microdevice exploits the inherent larger size of tumor cells and captures EpCAM positive and negative tumor cells. In addition, the ability to capture and characterize CTCs on a single platform simplifies the processing and prevents loss of cells, yielding high recovery rates. While the CellSearch assay may report higher number of cytokeratin-positive events, only a small proportion of these meet the strict definition of a CTC – an intact cell with DAPI-positive nucleus that is cytokeratin-positive and CD45- negative.

Discussion

Sensitive detection of rare CTC, a clinically relevant event in blood of cancer patients, has been a technical challenge, and in this report we demonstrate a possible solution utilizing a novel microfabricated parylene membrane filter device with simple manual syringe injection system for capturing CTC directly from human peripheral blood with minimal processing, which is capable of greater than 90% recovery with high enrichment factor (7 logs), outperforming the only FDA-approved method currently available to clinicians. Previously, we reported the ability to perform on-chip capture integrated with electrolysis for further downstream nucleic acid analysis (15) and here we have shown that we can further characterize the cells on-chip by immunofluorescence. We have demonstrated superior recovery rate in comparison to the FDA-approved Cellsearch® system, and CTC recovery also appears superior to a recently described affinity-based microchip system that also uses antibody-based separation (7) based on the reported recovery rates using spiked model system. We have demonstrated the feasibility of using our microdevice to assay clinical specimens. Finally, standard microfabrication processes can ensure uniform manufacturing and the fact that antibodies are not required for enrichment of CTC, should provide lower cost per device, translating into lower assay costs for the patients and healthcare industry. The clinical utility of this technology can only be assessed in prospective multi-institutional clinical trials and in comparative studies with established, FDA approved technologies for CTC analysis, studies we are currently undertaking. These would move us towards analytical validation of this technology. The simplicity and portability of the microdevice provides for the potential to be incorporated as a routine clinical test. While it remains to be proven in a prospective clinical trial which we are in the process of, the CTC capture step can be performed at the bedside or office without additional equipment; thereby providing widespread access to this technology without large capital equipment outlays. This novel portable filter-based CTC enrichment microdevice could provide a cost-effective method to detect CTC with higher recovery rate for assaying metastasis, and should also be useful in monitoring therapeutic response in patients. Because virtually all solid tumors, including those of epithelial origin, are larger than the vast majority of normal cells of the blood (even small cell lung tumors are 1.5x – 4x the size of a lymphocyte (18), the microdevice should have much broader application than affinity based methods, which can only capture cells expressing high levels of the capture antigen. In initial assessments, the platform appears to provide reproducible results; our initial results from 3 independent operators yielded similar recovery rates from spiking experiments, but further studies will need to be performed. The platform has the potential to perform repeat tumor “biopsies” in patients undergoing cancer therapy through a simple blood test. The microdevice provides a single station capture, enrichment and molecular analysis tool for characterization of CTC, allowing for identification of therapeutic targets directly on the captured CTC. It is also clear that the device we have described could have utility for a variety of applications in which size based separation might be clinically important.

Statement of Translational Relevance

The detection of circulating tumor cells (CTC) in the blood of cancer patients is a critically important issue with vast implications to the study and treatment of cancer. It has been demonstrated that CTC indicate disease progression and can be used to monitor therapeutic response. However, a major problem in the field has been the lack of sensitive and efficient methods to capture and analyze CTC. This filter-based portable microdevice exploits the differences between size of the larger epithelial CTC and the smaller hematopoietic cells and allows for efficient capture of CTC, followed by their on-chip analysis. The portable system we describe here allows for speedy bedside or in-office processing to circumvent the need for transportation to a central processing

facility. Such a portable device with high CTC recovery rates and ease of post-capture analysis has the potential to revolutionize the field of CTC detection and analysis.

Acknowledgments

The authors thank participating patients for the source of clinical blood samples.

Grant Support This work was supported in part by National Institutes of Health Grant 1R21CA123027-01, Doheny Eye Institute Specialized Imaging Core grant EY03040.

References

1. Lugo TG, Braun S, Cote RJ, Pantel K, Rusch V. Detection and measurement of occult disease for the prognosis of solid tumors. *J Clin Oncol*. 2003; 21:2609–15. [PubMed: 12829682]
2. Schabel FM Jr. Rationale for adjuvant chemotherapy. *Cancer*. 1977; 39:2875–82. [PubMed: 141322]
3. Pantel K, Alix-Panabieres C, Riethdorf S. Cancer micrometastases. *Nat Rev Clin Oncol*. 2009
4. Scher HI, Jia X, de Bono JS, et al. Circulating tumour cells as prognostic markers in progressive, castration-resistant prostate cancer: a reanalysis of IMMC38 trial data. *Lancet Oncol*. 2009; 10:233–9. [PubMed: 19213602]
5. Cristofanilli M, Budd GT, Ellis MJ, et al. Circulating tumor cells, disease progression, and survival in metastatic breast cancer. *N Engl J Med*. 2004; 351:781–91. [PubMed: 15317891]
6. Maheswaran S, Sequist LV, Nagrath S, et al. Detection of mutations in EGFR in circulating lung-cancer cells. *N Engl J Med*. 2008; 359:366–77. [PubMed: 18596266]
7. Nagrath S, Sequist LV, Maheswaran S, et al. Isolation of rare circulating tumour cells in cancer patients by microchip technology. *Nature*. 2007; 450:1235–9. [PubMed: 18097410]
8. de Bono JS, Scher HI, Montgomery RB, et al. Circulating tumor cells predict survival benefit from treatment in metastatic castration-resistant prostate cancer. *Clin Cancer Res*. 2008; 14:6302–9. [PubMed: 18829513]
9. Paterlini-Brechot P, Benali NL. Circulating tumor cells (CTC) detection: Clinical impact and future directions. *Cancer Lett*. 2007
10. Rosenberg R, Gertler R, Friederichs J, et al. Comparison of two density gradient centrifugation systems for the enrichment of disseminated tumor cells in blood. *Cytometry*. 2002; 49:150–8. [PubMed: 12454978]
11. Lara O, Tong XD, Zborowski M, Chalmers JJ. Enrichment of rare cancer cells through depletion of normal cells using density and flow-through, immunomagnetic cell separation. *Experimental Hematology*. 2004; 32:891–904. [PubMed: 15504544]
12. Vona G, Sabile A, Louha M, et al. Isolation by size of epithelial tumor cells - A new method for the immunomorphological and molecular characterization of circulating tumor cells. *American Journal Of Pathology*. 2000; 156:57–63. [PubMed: 10623654]
13. Becker FF, Wang XB, Huang Y, Pethig R, Vykoukal J, Gascoyne PR. Separation of human breast cancer cells from blood by differential dielectric affinity. *Proc Natl Acad Sci U S A*. 1995; 92:860–4. [PubMed: 7846067]
14. Shaffer DR, Leversha MA, Danila DC, et al. Circulating tumor cell analysis in patients with progressive castration-resistant prostate cancer. *Clin Cancer Res*. 2007; 13:2023–9. [PubMed: 17404082]
15. Zheng S, Lin H, Liu JQ, et al. Membrane microfilter device for selective capture, electrolysis and genomic analysis of human circulating tumor cells. *J Chromatogr A*. 2007; 1162:154–61. [PubMed: 17561026]
16. Meng S, Tripathy D, Frenkel EP, et al. Circulating tumor cells in patients with breast cancer dormancy. *Clin Cancer Res*. 2004; 10:8152–62. [PubMed: 15623589]
17. Went PT, Lugli A, Meier S, et al. Frequent EpCam protein expression in human carcinomas. *Human pathology*. 2004; 35:122–8. [PubMed: 14745734]

18. Lee TK, Esinhart JD, Blackburn LD, Silverman JF. The size of small cell lung carcinoma cells. Ratio to lymphocytes and correlation with specimen size and crush artifact. *Anal Quant Cytol Histol.* 1992; 14:32–4. [PubMed: 1313679]

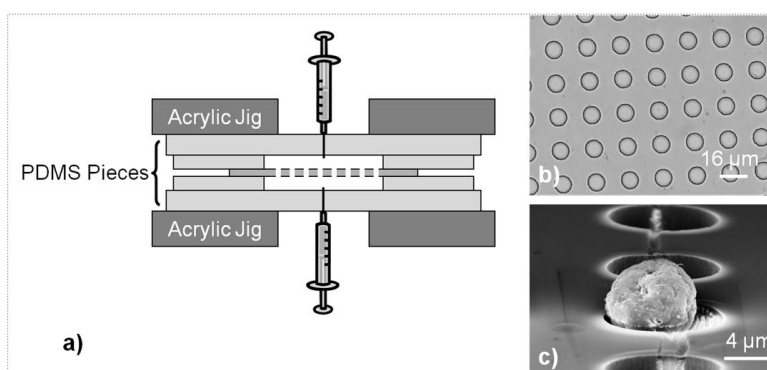


Figure 1.

Illustration of device assembly. a) Schematic drawing of a functional microdevice consists of parylene membrane filter sandwiched between rectangular PDMS slabs and clamped in between acrylic jigs with inlet and outlet for syringes. b) Bright field image of an optically transparent parylene filter with uniformly shaped and spaced 8 μm pores. c) SEM picture of single cultured tumor cell captured on the membrane.

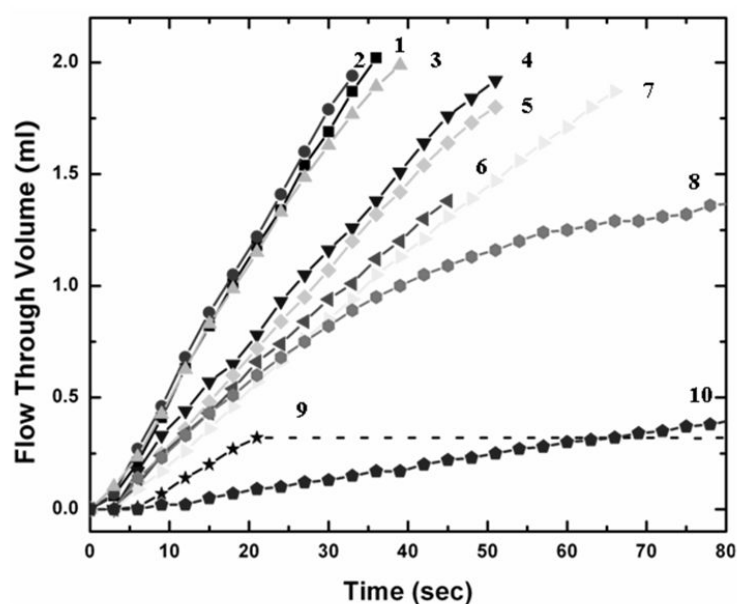


Figure 2.

Flow characterization of the microdevices with varying sample composition under constant pressure of 0.5 psi.

1. PBS only (square);
2. PBS with 50k LNCaP cells (circle);
3. PBS with 50k LNCaP cells fixed in 1% acetone (triangle);
4. 50% human blood (triangle);
5. 50% human blood with 25k LNCaP cells (square);
6. 50% blood fixed in 1% NBF (triangle);
7. 50% blood and 25k LNCaP cells fixed in 1% NBF (triangle);
8. 50% blood and 25k LNCaP cells fixed in 2% NBF (hexagon);
9. 50% blood and 25k LNCaP cells fixed in 5% NBF. Dash line part of curve 9 was caused by severe blocking of filter so that the filtration could not be completed (star);
10. 100% human blood (pentagon).

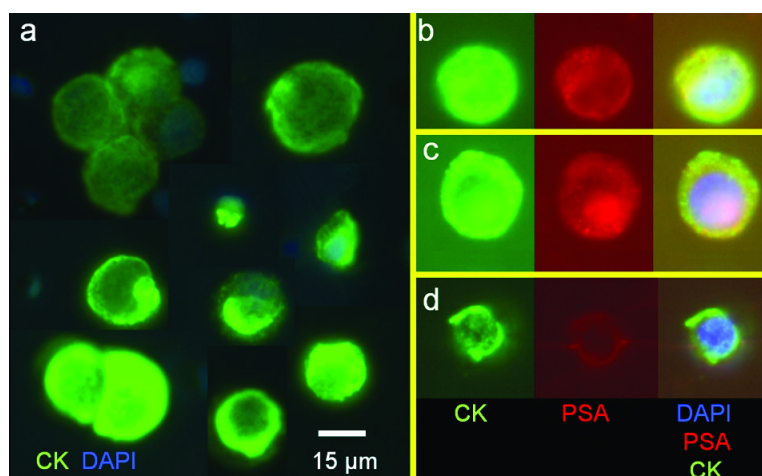


Figure 3.

On-Chip capture and immunofluorescent (IF) testing of captured tumor cells. a) Montage of captured tumor cell lines (model system), showing expression of CK (green) by IF (with DAPI nuclear counterstain, blue); note the size heterogeneity within the model system. b) and c) CK positive/PSA positive and d) CK positive/PSA negative CTCs captured from the peripheral blood of a patient with prostate cancer. CK positive cells are green, PSA positive cells are red. When both CK and PSA are expressed, the combined color is yellow.

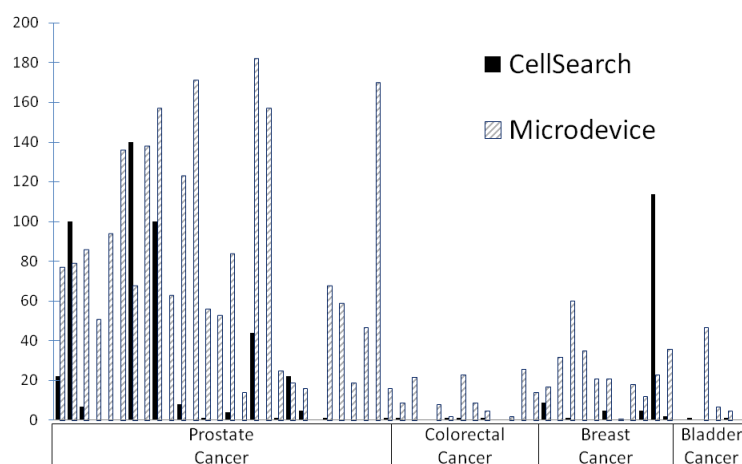


Figure 4. Histogram demonstrating performance comparison of membrane microfilter vs. CellSearch® assay in clinical samples. Solid and striped bars denote number of CTCs detected using the commercially available CellSearch® assay and microdevice, respectively. The number of CTC positive samples were 27 vs. 14 (microdevice vs. CellSearch®) out of 28 patients for prostate cancer, 10 vs. 4 out of 12 patients for colorectal cancer, 11 vs. 6 out of 11 patients for breast cancer and 4 vs. 3 out of 6 patients for bladder cancer.

Table 1

List of samples and CTC counts per 7.5 ml of blood using the CellSearch® and Microdevice methods.

Sample	Cancer Type	CTC/7.5ml CellSearch®	CTC/7.5mL Microdevice
1	Prostate	22	77
2	Prostate	100	79
3	Prostate	7	86
4	Prostate	0	51
5	Prostate	0	94
6	Prostate	0	136
7	Prostate	140	68
8	Prostate	0	138
9	Prostate	100	157
10	Prostate	0	63
11	Prostate	8	123
12	Prostate	0	171
13	Prostate	1	56
14	Prostate	0	53
15	Prostate	4	84
16	Prostate	0	14
17	Prostate	44	182
18	Prostate	0	157
19	Prostate	1	25
20	Prostate	22	19
21	Prostate	5	16
22	Prostate	0	0
23	Prostate	1	68
24	Prostate	0	59
25	Prostate	0	19
26	Prostate	0	47
27	Prostate	0	170
28	Prostate	1	16
29	Colorectal	22	9
30	Colorectal	0	22
31	Colorectal	0	0
32	Colorectal	0	8
33	Colorectal	1	2
34	Colorectal	1	23
35	Colorectal	0	9
36	Colorectal	1	5

Sample	Cancer Type	CTC/7.5ml CellSearch®	CTC/7.5mL Microdevice
37	Colorectal	0	0
38	Colorectal	0	2
39	Colorectal	0	26
40	Colorectal	0	14
41	Breast	9	17
42	Breast	0	32
43	Breast	1	60
44	Breast	0	35
45	Breast	0	21
46	Breast	5	21
47	Breast	0	1
48	Breast	0	18
49	Breast	5	12
50	Breast	114	23
51	Breast	2	36
52	Bladder	0	0
53	Bladder	1	0
54	Bladder	0	47
55	Bladder	0	7
56	Bladder	1	5
57	Bladder	0	0

Focus grid generation by in-line holography

Jigang Wu,^{1,*} Lap Man Lee,² and Changhui Yang^{1,2}

¹*Department of Electrical Engineering, California Institute of Technology, 1200 E California Blvd., Pasadena, CA 91125, USA*

²*Department of Bioengineering, California Institute of Technology, 1200 E California Blvd., Pasadena, CA 91125, USA*

**jigang@caltech.edu*

Abstract: We describe a simple way to generate a wide-area high-resolution focus grid by in-line holography and study the factors that impacts its quality. In our holographic recording setup, the reference beam was the direct transmission of the incoming collimated laser beam through a mask coating with thin metal film, and the sample beam was the transmission of the laser through small apertures fabricated on the mask. The interference of the two beams was then recorded by a holographic plate positioned behind the mask. Compared with other recording schemes, the in-line holography scheme has many distinct advantages and is more suitable for generating a wide-area focus grid. We explored the dependence of diffraction quality, including reconstructed focus spot intensity and spot size, on different parameters for recording, such as optical density of the metal film, size of the apertures, and focal lengths. A wide-area focus grid (170 x 138 spots with area 5.1 mm x 4.1 mm) was recorded using the in-line holography scheme for a demonstration.

©2010 Optical Society of America

OCIS codes: (090.0900) Holography; (090.2890) Holographic optical element.

References and links

1. R. Gräf, J. Rietdorf, and T. Zimmermann, "Live cell spinning disk microscopy," *Adv. Biochem. Eng. Biotechnol.* **95**, 57–75 (2005).
 2. J. Bowersdorf, R. Pick, and S. W. Hell, "Multifocal multiphoton microscopy," *Opt. Lett.* **23**(9), 655–657 (1998).
 3. P. M. Lundquist, C. F. Zhong, P. Zhao, A. B. Tomaney, P. S. Peluso, J. Dixon, B. Bettman, Y. Lacroix, D. P. Kwo, E. McCullough, M. Maxham, K. Hester, P. McNitt, D. M. Grey, C. Henriquez, M. Foquet, S. W. Turner, and D. Zaccarin, "Parallel confocal detection of single molecules in real time," *Opt. Lett.* **33**(9), 1026–1028 (2008).
 4. J. Ho, A. V. Parwani, D. M. Jukic, Y. Yagi, L. Anthony, and J. R. Gilbertson, "Use of whole slide imaging in surgical pathology quality assurance: design and pilot validation studies," *Hum. Pathol.* **37**(3), 322–331 (2006).
 5. M. Oheim, "High-throughput microscopy must re-invent the microscope rather than speed up its functions," *Br. J. Pharmacol.* **152**(1), 1–4 (2007).
 6. J. Wu, X. Cui, G. Zheng, Y. M. Yang, L. M. Lee, and C. Yang, "A wide field-of-view microscope based on holographic focus grid illumination," (accepted by *Opt. Lett.*).
 7. F. Kalkum, S. Broch, T. Brands, and K. Buse, "Holographic phase conjugation through a sub-wavelength hole," *Appl. Phys. B* **95**(3), 637–645 (2009).
 8. W. Liu, and D. Psaltis, "Pixel size limit in holographic memories," *Opt. Lett.* **24**(19), 1340–1342 (1999).
 9. D. Gabor, "A new microscopic principle," *Nature* **161**(4098), 777–778 (1948).
 10. J. J. Barton, "Removing multiple scattering and twin images from holographic images," *Phys. Rev. Lett.* **67**(22), 3106–3109 (1991).
 11. W. Xu, M. H. Jericho, I. A. Meinertzhagen, and H. J. Kreuzer, "Digital in-line holography for biological applications," *Proc. Natl. Acad. Sci. U.S.A.* **98**(20), 11301–11305 (2001).
 12. V. Moreno, J. F. Roman, and J. R. Salgueiro, "High efficiency diffractive lenses: deduction of kinoform profile," *Am. J. Phys.* **65**(6), 556–562 (1997).
 13. M. H. Horman, and H. H. M. Chau, "Zone plate theory based on holography," *Appl. Opt.* **6**(2), 317–322 (1967).
 14. J. W. Goodman, *Introduction to Fourier Optics* (Roberts & Company Publishers, 3rd edition, 2004), Chap. 9.
 15. C. Genet, and T. W. Ebbesen, "Light in tiny holes," *Nature* **445**(7123), 39–46 (2007).
 16. A. K. Richter, and F. P. Carlson, "Holographically generated lens," *Appl. Opt.* **13**(12), 2924–2930 (1974).
 17. H. I. Bjelkhagen, *Silver-halide recording materials for holography and their processing* (Springer, 2nd edition, 1995), Chap. 5.
-

1. Introduction

Focus grid illuminations has been used for multi-beam confocal microscopy [1], multifocal microscopy [2], and single molecule detection [3], etc. In such applications, it is important to generate a tight focus spot for high-resolution imaging, and a small spacing between the focus spots for fast image acquisition speed. Previously, the focus grid is usually generated by using microlens array, diffractive optical elements, or holographic optical elements, along with a microscope objective to achieve the abovementioned characteristics. One disadvantage of these methods is that the area of the focus grid illumination will be limited by the field-of-view of microscope objective, and is thus unsuitable for applications that require wide field-of-view imaging, e.g., whole-slide imaging [4] or high-throughput imaging and sensing [5]. Obviously, to achieve a wider field-of-view, the microscope objective has to be eliminated when generating the focus grid illumination.

An appropriately designed microlens array provides a good alternate solution. The number of elements in such an array can be scaled up arbitrarily. However, there is a significant downside to such a solution – the grid density is typically low. This is because the required numerical apertures for high resolution spots ($< 1\ \mu\text{m}$) necessarily require the focus spot separation and the focal length to be high. For example, to accomplish a focused spot size of $1\ \mu\text{m}$ at a focal distance of $10\ \text{mm}$, each microlens in the array would have to be at least $5\ \text{mm}$ in diameter (assuming wavelength of $500\ \text{nm}$). Since the pitch of the focus grid is equal to microlens' diameter, this implies that such an array would have a pitch of $5\ \text{mm}$. This sparse grid density is a significant impediment for most applications. The grid density can potentially be increased by using smaller lenses with shorter focal lengths. However, the required optical surfaces would be more difficult to fabricate and the shorter focal lengths may be restrictive for certain applications.

Interestingly, it is worth noting that the physical lenses are not the only means by which we can focus light. It is also possible to implement a virtual microlens array via holographic recording. An appropriately patterned piece of holographic plate should be able to transform a uniform input coherent light field into a grid of tightly focused light spots. The holographic projection-base approach has two advantages. First, implementation would be simpler and cheaper, as long as we can write the appropriate pattern into the holographic plate. Second, the effective holographic lenses can 'overlap' to a great extent, and, as such, we would be able to achieve a higher focus grid density. Recently, we showed that an appropriately patterned holographic plate can generate light spots of diameter $0.74\ \mu\text{m}$ at a focal distance of $6\ \text{mm}$ with a pitch of $30\ \mu\text{m}$ [6]. The corresponding holographic lens diameter is $4.3\ \text{mm}$. This implies that the lens overlap ratio (lens diameter divided by pitch) is 140 (for conventional lenslet array, this ratio is at most 1).

The use of holography to generate a high-resolution focus spot has been demonstrated by several groups via well-designed schemes [7, 8]. In their schemes, the transmission of a tiny aperture was interfered with a reference beam and recorded by holographic materials. This approach can provide high-quality and well-controlled recording.

In-line holography was originally proposed by Gabor more than half a century ago [9] and has been studied extensively since then [10, 11]. In this paper, we show that an in-line holography scheme can be used for generating a wide-area focus grid. In our scheme, as shown in Fig. 1(a), the direct transmission of a collimated laser beam through a semi-transparent mask interferes with the transmission of the laser through an aperture grid fabricated on the semi-transparent mask, and the interference pattern is recorded by a holographic plate. The advantages of our scheme can be summarized as follows: (1) The in-line scheme make the setup insensitive to vibrations and perturbations in the system; (2) The focal length of the focus grid can be adjusted easily and can be short with relative ease; (3) The scheme is suitable for recording large-area aperture grid and thus suitable for achieving large-area focus grid. This paper reports our experimental findings regarding the impact of various implementation parameters on the quality of the recording.

The quality of the holographic recording depends on the aperture size, the opacity of the mask and the focal length. The parameter choices for creating an optimal recording are not apparent by simply dissecting the problem analytically. Here, we experimentally show the impact of each major design choice on the recording's properties. This paper will hopefully serve as a guide for researchers looking to create such holographic grids for their respective experiments.

In section 2, we will describe the in-line holography setup for recording the hologram for generating a focus grid and present a theory for calculating the reconstructed focus spot intensity. In section 3, we show a series of experiment that studies the dependence of hologram quality, including reconstructed spot size and diffraction efficiency, on experiment parameters, such as optical density (OD) of the mask, the aperture size, and the focal length. Finally, we summarize our work in section 4.

2. In-line holography setup

The in-line holography setup for recording a hologram that can generate a focus spot (a holographic lens) is shown in Fig. 1(a). The holographic lens is also called a sinusoidal zone plate [12] or a Garbor zone plate [13]. The mask in the setup consists of an aperture patterned on a layer of metal film. When a collimated laser beam shines on the mask, the transmission through the aperture serves as sample wave. The metal film is deliberately made to be thin so that the collimated laser beam can directly transmit through it and be attenuated. The direct transmission of the beam through the metal film then serves as reference wave and interferes with the sample beam and the interference is recorded by a holographic plate positioned at a certain distance behind the mask. In the experiment, we used a silver halide holographic plate.

After exposure, the holographic plate was developed and bleached to produce a phase hologram. A focus spot can then be generated by the holographic reconstruction process, as shown in Fig. 1(b), where a conjugated collimated beam is transformed into a focus spot by the hologram. The focal length of the holographic lens is the same as the distance between the mask and the holographic plate during the recording process.

By replacing the mask with one that is patterned with a grid of apertures, the same process will yield a phase hologram that can render a grid of focus spots.

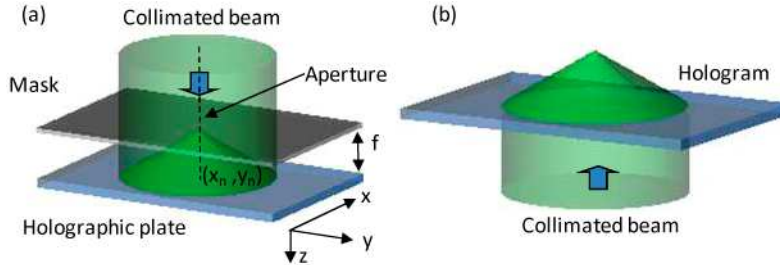


Fig. 1. In-line holography scheme for fabricating a holography lens. (a) Recording of the hologram; (b) Reconstruction of the focus spot.

Considering the sensitivity dynamic range of holographic materials, it is preferable to make the intensity of reference beam comparable to that of the sample beam. This is true if we have only one aperture on the mask. However, for aperture grid on the mask, the interference between the transmissions of different apertures will contribute to the hologram pattern and affect diffraction if the transmissions are comparable to the reference beam transmission. Thus in the recording scheme, it is important to make the intensity of the reference beam much stronger than that of the sample beam so that a reasonable reconstruction can be achieved [14].

The transmission through tiny apertures is generally a complicated problem and defies simple solution without some approximations [15]. An approximate theory for calculating holographically generated lens can be found in Ref [16], where the Fraunhofer diffraction was used to approximate the transmission through the aperture. Similar to Ref [13], our

calculation below is based on the simpler assumption that the sample beam is a combination of spherical waves and the reference beam is a plane wave, since the apertures in our experiment is comparable to the wavelength and much smaller than the focal length. Using paraxial approximation, the sample wave, i.e., the transmission through the aperture grid, can be written as

$$\frac{A_1}{f} \sum_n \exp\left(i \frac{\pi}{f\lambda} [(x-x_n)^2 + (y-y_n)^2]\right) \quad (1)$$

where f is the focal length, A_1/f is the amplitude of one hole, (x_n, y_n) is the coordinate of the center of the aperture n , and λ is the laser wavelength. Here we neglect the constant phase shift from propagation along z -direction. Figure 1(a) shows the scheme with aperture n . Thus the interferogram intensity on the holographic plate can be written as:

$$\begin{aligned} I(x) &\approx \left| A_0 + \frac{A_1}{f} \sum_n \exp\left(i \frac{\pi}{f\lambda} [(x-x_n)^2 + (y-y_n)^2]\right) \right|^2 \\ &= A_0^2 + 2A_0 \frac{A_1}{f} \sum_n \cos\left(\frac{\pi}{f\lambda} [(x-x_n)^2 + (y-y_n)^2]\right) \\ &\quad + \frac{A_1^2}{f^2} \sum_n \exp\left(i \frac{\pi}{f\lambda} [(x-x_n)^2 + (y-y_n)^2]\right) \sum_n \exp\left(-i \frac{\pi}{f\lambda} [(x-x_n)^2 + (y-y_n)^2]\right) \\ &\approx A_0^2 + 2A_0 \frac{A_1}{f} \sum_n \cos\left(\frac{\pi}{f\lambda} [(x-x_n)^2 + (y-y_n)^2]\right) \end{aligned} \quad (2)$$

where A_0 is reference wave amplitude. Here we use the approximation that $A_1 \ll A_0$.

After developing and bleaching, we will get a phase hologram [17] and the transmission can be written as

$$\begin{aligned} t(x) &= \exp\left[iK \left(A_0^2 + 2A_0 \frac{A_1}{f} \sum_n \cos\left(\frac{\pi}{f\lambda} [(x-x_n)^2 + (y-y_n)^2]\right) \right)\right] \\ &= \exp(iKA_0^2) \prod_n \exp\left[i\beta \cos\left(\frac{\pi}{f\lambda} [(x-x_n)^2 + (y-y_n)^2]\right)\right] \end{aligned} \quad (3)$$

where K is a constant, and $\beta = 2KA_0A_1/f$ is the modulation amplitude. The modulation term can be further expanded as

$$\exp\left[i\beta \cos\left(\frac{\pi}{f\lambda} [(x-x_n)^2 + (y-y_n)^2]\right)\right] = \sum_{l=-\infty}^{\infty} (i)^l J_l(\beta) \exp\left[i l \frac{\pi}{f\lambda} [(x-x_n)^2 + (y-y_n)^2]\right] \quad (4)$$

where $J_l(\beta)$ is the l th order Bessel function of the first kind. When β is small and $l \geq 0$,

$$J_l(\beta) \approx \frac{1}{\Gamma(l+1)} \left(\frac{\beta}{2}\right)^l \quad (5)$$

Neglecting higher order terms, we have

$$\begin{aligned}
& \exp \left[i\beta \cos \left(\frac{\pi}{f\lambda} [(x-x_n)^2 + (y-y_n)^2] \right) \right] \\
& \approx J_0(\beta) + iJ_1(\beta) \exp \left[i \frac{\pi}{f\lambda} [(x-x_n)^2 + (y-y_n)^2] \right] + iJ_{-1}(\beta) \exp \left[-i \frac{\pi}{f\lambda} [(x-x_n)^2 + (y-y_n)^2] \right] \quad (6) \\
& \approx 1 + \frac{i\beta}{2\Gamma(2)} \exp \left[i \frac{\pi}{f\lambda} [(x-x_n)^2 + (y-y_n)^2] \right] + \frac{i\beta}{2\Gamma(2)} \exp \left[-i \frac{\pi}{f\lambda} [(x-x_n)^2 + (y-y_n)^2] \right]
\end{aligned}$$

where we use the relation $J_{-1}(\beta) = J_1(\beta)$. Thus Eq. (3) becomes

$$\begin{aligned}
t(x) & \propto \prod_n \left(1 + \frac{i\beta}{2\Gamma(2)} \exp \left[i \frac{\pi}{f\lambda} [(x-x_n)^2 + (y-y_n)^2] \right] + \frac{i\beta}{2\Gamma(2)} \exp \left[-i \frac{\pi}{f\lambda} [(x-x_n)^2 + (y-y_n)^2] \right] \right) \quad (7) \\
& \approx 1 + \frac{i\beta}{2\Gamma(2)} \sum_n \exp \left[i \frac{\pi}{f\lambda} [(x-x_n)^2 + (y-y_n)^2] \right] + \frac{i\beta}{2\Gamma(2)} \sum_n \exp \left[-i \frac{\pi}{f\lambda} [(x-x_n)^2 + (y-y_n)^2] \right]
\end{aligned}$$

We neglect higher order terms in this analysis. The first term corresponds to the 0 order of the transmitted beam, and the second and third terms correspond to the +1 and -1 order of the diffraction. Comparing with Eq. (1), we can see that the +1 and -1 order diffraction will generate the focus grid and its conjugate image. The amplitude of the +1 order diffraction, which is the diffraction order that we are interested, can be written as

$$\left| \frac{i\beta}{2\Gamma(2)} \right|^2 \propto \beta^2 \propto A_0^2 A_1^2 / f^2 \quad (8)$$

Thus, the reconstructed focus spot intensity will be proportional to the intensity of reference beam, the intensity of sample beam behind the mask, and inversely proportional to the square of focal length. Note that the above equation is an approximation and is not valid for comparable reference and sample beam intensities.

For the focus spot size, a perfectly reconstructed focus spot will be comparable in size to the original aperture in the mask. However, for small apertures that are comparable to the wavelength, the reconstructed spot size will also depend on other factors, such as the resolution of the holographic material, uniformity of the holographic emulsion, the focal length, and the relative intensity between sample and reference beams.

In the next section, we show the result of a series of experiment, where we fabricated holograms using masks with different ODs, different sizes of the apertures, and different focal lengths. The experimental results agree well with the above theoretical analysis.

3. Experiments and Analysis

In the experiment, we used chrome masks with OD = 2.1, 3.2, 4.2, and 5.3. A line of apertures were punched through the metal film on each mask using focused ion beam, and the sizes of the apertures were 0.2, 0.4, 0.6, 0.8, 1.0, 1.2, 1.4, 1.6, 1.8, and 2.0 μm . The separation between adjacent apertures was 60 μm . For each mask, holograms were recorded at focal lengths of $f = 3, 6, 9, 12$ mm. We used a green laser with wavelength of 532 nm and power of 200 mW (Excelsior-532-200, Spectra-Physics) for recording the hologram. The holographic material was silver halide (VRP, Integraf). In the reconstruction, we set the intensity of the collimated beam incident on the hologram to be 17 $\mu\text{W}/\text{cm}^2$.

With increasing ODs, the reference beam was attenuated more and the intensity was closer to that of the sample beam. According to the previous discussion, we should expect to see better diffraction and stronger focus spots for larger OD, since the intensities of the sample beam will be more comparable to that of the reference beam. So it is not surprising that for OD 2.1, and 3.2, the reconstructed spots can be observed clearly for all the aperture sizes except 0.2 μm , and for OD 4.2, all the reconstructed spots can be observed. However, for OD 5.3, we can observe multiple diffractions of the hologram, which prevent a clear correspondence between focus spots and the apertures on the mask.

Figure 2 shows the microscope image of masks and reconstructed spots of holograms with OD 4.2 and OD 5.3. Figure 2(a), 2(b) show the images for OD-4.2 mask, where the reconstructed spots is an exact replication of the apertures. Figure 2(c), 2(d) show the images for OD-5.3 mask, where we can see that the number of reconstructed spots is more than that of the apertures. This is because for OD 5.3, the interference between the transmissions of different apertures is comparable to the interference between the transmission of apertures and the reference beam. Thus unwanted interference between the aperture transmissions would be patterned onto the hologram and prevent a clearly reconstruction of the focus spots that correspond to the original apertures. For OD 2.1, 3.2 and 4.2, the intensity of reference beam is much higher than that of the sample beam, and the correspondence of reconstructed focus spots and original apertures can be clearly seen.

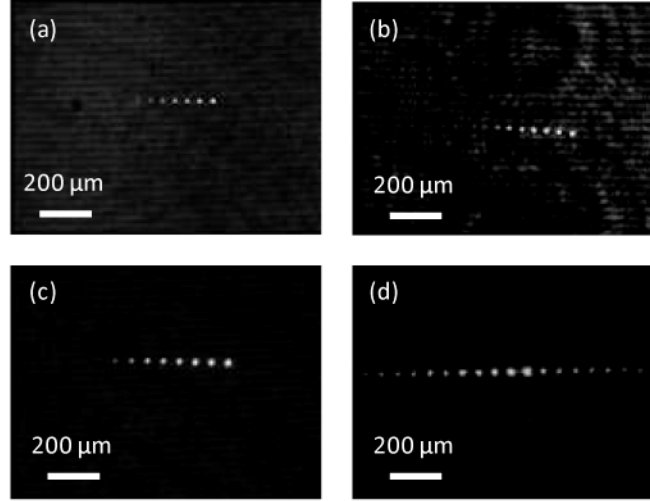


Fig. 2. Microscope image of masks and reconstructed spots of holograms under 4X objective. (a) Mask with OD 4.2; (b) Reconstructed spots of hologram corresponding to OD-4.2 mask; (c) Mask with OD 5.3; (d) Reconstructed spots of hologram corresponding to OD-5.3 mask.

The reconstructed spot intensities and the full-width-half-maximum (FWHM) spot sizes were measured, using a microscope with 60X/NA0.95 objective, for OD 2.1, 3.2, and 4.3 and plotted in Fig. 3, where Fig. 3(a), 3(b) show the plots for OD 2.1, Fig. 3(c), 3(d) show the plots for OD 3.2, and Fig. 3(e), 3(f) show the plots for OD 4.3. From Fig. 3(a), 3(c), and 3(e), we can observe the following important features regarding the reconstructed spot intensity:

- (I1) For same OD and same focal length, the reconstructed spot intensity decreases with smaller aperture size. This could be explained by less transmission through smaller apertures and Eq. (8).
- (I2) The reconstructed spot intensity is roughly inversely proportional to the attenuation coefficient of reference beam through the mask, and thus stronger for larger OD. This is because in the experiment, the total exposure on the holographic plate is set to be the optimal value of $80 \mu\text{J}/\text{cm}^2$ for the holographic material VRP. Assuming that the reference beam intensity is much larger than the sample beam intensity, the increase in OD of the mask will result in increase in sample beam exposure during recording as the exposure time will be longer. Thus according to Eq. (8), the spot intensity will increase to the same amount as OD decreases. The experiment shows that for the same aperture size, the spot intensities of OD-3.2 holograms are roughly 10 times of the spot intensities of OD-2.1 holograms, and the spot intensities of OD-4.2 holograms are roughly 5-8 times of the spot intensities of OD-3.2 holograms. This agrees well with the theory

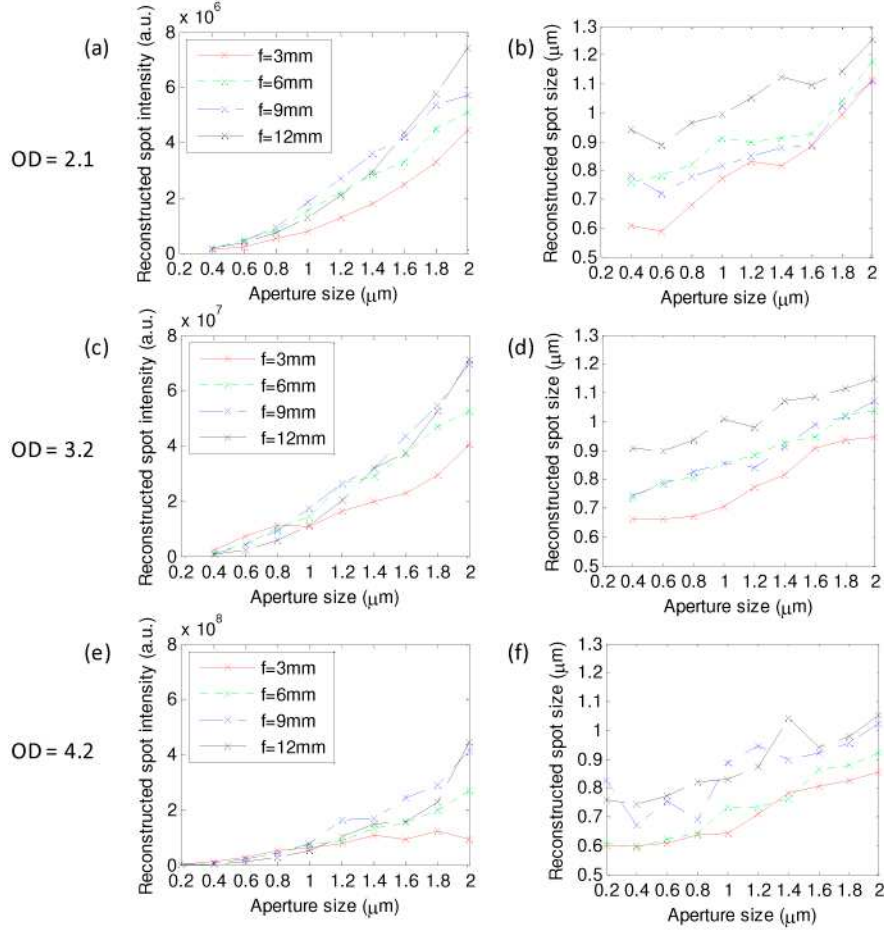


Fig. 3. Reconstructed spot intensity and FWHM spot size versus aperture size at different ODs and different focal lengths. (a)(b) OD = 2.1; (c)(d) OD = 3.2; (e)(f) OD = 4.2.

From Fig. 3(b), 3(d), and 3(f), we can observe the following important features regarding reconstructed spot size:

- (S1) For same OD and same aperture, the spot size decreases with smaller focal length. This could be explained by the effective holographic lens area on the hologram. As the focal length decreases, the effective holographic lens area also decreases, thus the impact of possible non-uniformity of the holographic recording material on the lens quality would be less, and the reconstructed spot size can be closer to the original aperture size.
- (S2) For same OD and same focal length, the spot size decreases with smaller aperture size and finally reaches an asymptotic value. The decrease in spot size is consistent with our logical expectation. The existence of an asymptotic value is unsurprising as well – the holographic material can only record feature size down to a certain limit. Reconstruction of a small spot requires the patterning of finer diffraction features. Once we have reached that limit, we cannot expect the reconstruction spot size to taper to an asymptotic value and any further decrease in the mask's aperture size would have no impact.

We can see that the reconstruction spot can have an FWHM spot size as small as $0.6\ \mu\text{m}$. Note that this can be smaller than the aperture diameter since we measured the FWHM spot size, which was related to the diffraction of the aperture.

(S3) For different OD and same aperture size, we can obtain similar reconstructed spot size, especially for small apertures and small focal lengths. This indicates that the spot size is less sensitive to the relative intensity between reference and sample beam, and more depending on the effective holographic lens area. This implies that the uniformity of the holographic material is an important quality-determining factor.

According to these experimental observations, we can see that to get an optimal hologram quality, we would first need to choose an optimal OD for the mask. An OD of 4 works well for holographic grid designs that are similar to the one we have here. We note that choosing an OD beyond 4 can potentially provide even better efficiency. However, an excessively high OD would significantly attenuate the reference intensity. In our experiments, the direct transmission through the mask becomes exceedingly weak for an OD beyond 5. In this situation, the diffraction transmissions through adjacent apertures would interfere significantly and lead to significant cross-talks.

Next an appropriate aperture size should be chosen according to (I1) and (S2), which show that there is a trade-off between spot intensity and spot size. Finally we can see that for small apertures, the spot intensity and spot size will generally get better as focal length decreases, thus we would want to choose the smallest possible focal length as long as it is compatible with the system design.

In the fabrication of our demonstration focus grid, we chose to use an aperture size of $0.8\ \mu\text{m}$ for small enough reconstructed spot size based on the reasons listed above. Figure 4 shows the reconstructed spot intensity vs. focal length and OD for the $0.8\text{-}\mu\text{m}$ aperture size. We can see that there is an optimal parameter set for getting the best spot intensity.

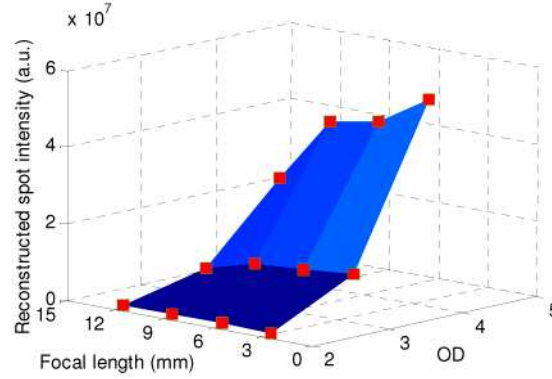


Fig. 4. Reconstructed spot intensity vs. focal length and OD for $0.8\text{-}\mu\text{m}$ aperture size. The squares indicate the experiment data points.

Using the in-line holography method, we fabricated a hologram that can generate a focus grid of 170×138 , with $30\text{-}\mu\text{m}$ separation between the focus spots. The hologram was recorded with an OD 4 mask with apertures of $0.8\text{-}\mu\text{m}$ diameter, and at a focal length of 5 mm. Figure 5 shows a small part of the reconstructed spots observed under microscope with a 20X objective. The FWHM spot size was measured to be around $0.7\ \mu\text{m}$. The focus grid can be readily used in a wide-field microscope system.

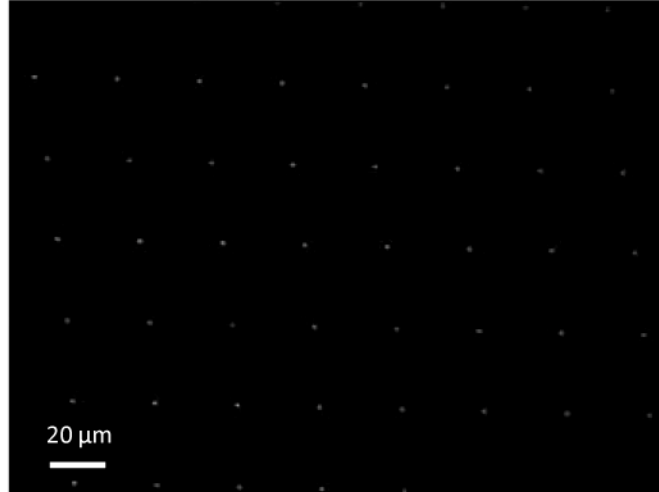


Fig. 5. Microscope image of a small part of the reconstructed focus grid under a 20X objective.

While this set of experiments did not study the impact of aperture separation on the focus grid quality, the observed dependency trends of the other design parameters can help inform us on this relationship. Specifically, an increase in grid density would lead to higher total transmissions through the apertures. This in turn would lead to more interference between the transmissions through different apertures. In this case, we expect a lower OD mask would be required so that the in-line holography interference is stronger than the cross-talk terms. The exact impact of aperture separation is well worth a future detailed experimental study.

4. Summary

In conclusion, we have shown an in-line holography scheme for recording a hologram to generate a wide-area focus grid. Compare with other methods for generating focus grid, our scheme is relatively simple, robust, and have many other advantages. We have studied the effect of mask OD, aperture size, and focal length on recording process and showed that a set of appropriate parameters is important for fabricating the hologram. A hologram was fabricated to generate a wide-area focus grid for demonstration of principle. The hologram can be potentially used for wide field-of-view imaging or parallel detecting and sensing applications.

Acknowledgement

The authors acknowledge Ying Min Wang, Guoan Zheng, and Dr. Xiquan Cui for helpful discussions. This work is supported by Department of Defense grant #W81XWH-09-1-0051.

Wide field-of-view microscope based on holographic focus grid illumination

Jigang Wu,^{1,*} Xiquan Cui,¹ Guoan Zheng,¹ Ying Min Wang,² Lap Man Lee,² and Changhui Yang^{1,2}

¹Department of Electrical Engineering, California Institute of Technology, 1200 E. California Boulevard, Pasadena, California 91125, USA

²Department of Bioengineering, California Institute of Technology, 1200 E. California Boulevard, Pasadena, California 91125, USA

*Corresponding author: jigang@caltech.edu

Received March 22, 2010; revised May 19, 2010; accepted May 29, 2010;
posted June 7, 2010 (Doc. ID 125762); published June 23, 2010

We have developed a new microscopy design that can achieve wide field-of-view (FOV) imaging and yet possesses resolution that is comparable to a conventional microscope. In our design, the sample is illuminated by a holographically projected light-spot grid. We acquire images by translating the sample across the grid and detecting the transmissions. We have built a prototype system with an FOV of $6\text{ mm} \times 5\text{ mm}$ and acquisition time of 2.5 s. The resolution is fundamentally limited by the spot size—our demonstrated average FWHM spot diameter was $0.74\text{ }\mu\text{m}$. We demonstrate the prototype by imaging a U.S. Air Force target and a lily anther. This technology is scalable and represents a cost-effective way to implement wide FOV microscopy systems. © 2010 Optical Society of America

OCIS codes: 170.0110, 090.2890, 170.5810.

Automated, high-resolution, and cost-effective wide field-of-view (FOV) microscopy is highly sought for many applications, such as high-throughput screening [1] and whole-slide digital pathology diagnosis [2]. In a conventional microscope, the FOV is inversely related to the microscope objective's resolution due to the critical requirement of aberration correction for the whole viewing area. Commercial products for accomplishing wide FOV imaging typically raster scan the target samples under microscope objectives and reconstitute full-view images from multiple smaller images. This approach requires precise mechanical actuation along two axes. Scaling up the FOV for such an approach requires a linear cost increase (add more objectives) or longer scan time. Recently, exciting in-line holography methods [3,4] demonstrated the potential to cover a wide FOV image very cost effectively and without requiring sophisticated optics and mechanical scanning. In-line holography does require excellent raw data quality, as data noise can significantly distort the computed image and deteriorate resolution. To our knowledge, in-line holography's demonstrated resolution for simple objects is about $1\text{ }\mu\text{m}$ [3].

In this Letter, we report a microscopy technique that employs holography concepts in a different fashion to accomplish wide FOV imaging. Our technique, termed holographic scanning microscopy (HSM), uses a specially written hologram to generate a grid of tightly focused light spots and uses this grid as illumination on the target sample to perform parallel multifocal scanning while the sample is translated across the grid. In comparison to in-line holography, the resolution here is fundamentally determined by the focused spot size. Unlike in-line holography, this approach does not require mechanical scanning, but the scanning format is a simple one-dimensional (1D) translation. This approach is readily scalable, as we would simply use a large hologram with more projection light spots to accomplish wider FOV imaging.

Our HSM prototype demonstration, as shown in Fig. 1(a), used a laser (Excelsior-532-200-CDRH, Spectra Physics, with wavelength of 532 nm and power of 200 mW) as light source. The laser was attenuated, spatial

filtered, and expanded to be a collimated Gaussian beam with $1/e^2$ beam diameter of 21.3 mm. We used the center portion of the beam (diameter 12 mm and power 1 mW) as the illumination. A hologram transferred the incoming collimated beam into a grid of 200×40 (along the x and the y direction, respectively) focused light spots at a focal length of 6 mm. The spacing between spots was $30\text{ }\mu\text{m}$. The sample was mounted on a translation stage (LTA-HS, Newport) and positioned under the illumination of the focus grid. An achromatic lens pair (MAP10100100-A, Thorlabs) imaged the focus grid onto the imaging sensor (MotionXtra N3 with 1280×1024 pixels and $12\text{ }\mu\text{m}$ pixel size, Integrated Design Tools) with a magnification of 1.6. Note that the aberration induced in the projection lenses is not critical since we only need to differentiate different focus spots, which were well separated ($30\text{ }\mu\text{m}$). A beam block with diameter of 1 mm was positioned at the focus of the lens pair to block the zero-order transmission through the hologram.

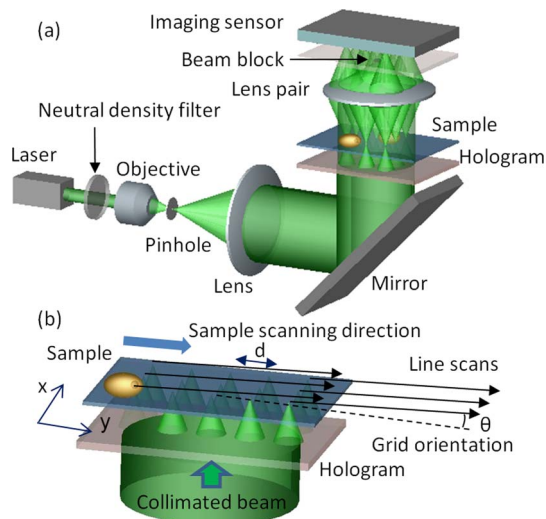


Fig. 1. (Color online) (a) System setup of the wide FOV microscope system and (b) scanning mechanism employed for imaging.

In the experiment, we linearly scanned the sample across the focus grid, which was tilted at a small angle with respect to the scanning direction, as shown in Fig. 1(b), and detected the transmission of the foci through the sample. Each focus spot will contribute to a line scan of the sample and a microscopic image can be reconstructed by appropriately shifting and assembling the line scans. This scanning scheme is similar to that of the optofluidic microscope [5], except that here we used a two-dimensional focus grid instead of a 1D aperture array. The focus grid was arranged so that the line scans of the adjacent columns of spots can be directly patched together. The linear scanning scheme has two advantages. First, we can achieve a small sampling distance of the image with relatively large focus spot spacing because of the slight angular tilt geometry. Second, it is simpler and can be much faster than a raster scanning scheme. As shown in Fig. 1(b), the sampling distances in the x and y directions can be written as

$$\delta x = d \sin(\theta), \quad \delta y = v/F, \quad (1)$$

where d is the spacing between focus spots, θ is the tilt angle of the focus grid with respect to the sample scanning direction, v is the scanning speed, and F is the frame rate of the imaging sensor. In the experiment, we chose the parameters to be $d = 30 \mu\text{m}$, $\theta = 0.025 \text{ rad}$, $v = 2.5 \text{ mm/s}$, and $F = 3333 \text{ frames/s}$. The exposure time was $7 \mu\text{s}$. Thus the sampling distances δx and δy were both $0.75 \mu\text{m}$, approximately matching the average focus spot size in our HSM system. Note that a high density of focused light spots is desirable as it would allow us to simultaneously collect more image data. On the other hand, we need to maintain adequate separation between adjacent light spots so that their projections on the sensor can be unambiguously distinguished. Our chosen spacing of $30 \mu\text{m}$ worked well as a compromise.

According to the scanning scheme, the FOV in the x direction is determined by the extent of focus spots in this direction. Because of the linear scanning characteristics, the starting and ending part of the image will have a sawtooth shape, as shown in Fig. 1(b). The effective FOV in the y direction can be calculated by $L - H$, where L is the scan length and H is the extent of focus spots in the y direction. We used 200×40 focused light spots with $30 \mu\text{m}$ spacing, and a scan length of 6.2 mm for acquiring our images. Thus the FOV was 6 mm in the x direction and 5 mm in the y direction. The acquisition time of the image is determined by the scanning speed and the range of the translation stage, and was calculated to be 2.5 s . We note that the FOV in the x direction can be expanded by simply adding more focused light spots along that direction through the use of a larger hologram. The FOV in the y direction is limited only by the extent to which we are willing to translate our sample along that direction.

The key optical component of our HSM system is the hologram. The use of holography to generate tiny focus spots has been reported in the literature [6,7]. Our hologram is technically challenging, as we require it to be capable of rendering tightly focused light spots over a relatively wide area. We implemented a scheme that is capable of patterning such a hologram [shown in Fig. 2(a)]. In this scheme, we employed a specially prepared mask. The mask consisted of a grid of apertures

patterned on a layer of metal film. The aperture diameter was $0.8 \mu\text{m}$, and the spacing between adjacent apertures was $30 \mu\text{m}$. The metal film was intentionally chosen to be thin (with an optical density of ~ 3) so that the incoming collimated light can be transmitted through it and be attenuated. The light transmitted through the apertures, serving as the sample beam, would then interfere with the attenuated collimated light, serving as the reference beam, and project an appropriate pattern onto the holographic plate (VRP, Integraf) for recording.

After exposure, the holographic plate was developed and bleached to produce the hologram. During reconstruction, as shown in Fig. 2(b), a conjugated collimated beam can then be transformed into a focus grid, and the focal length is the same as the distance between the holographic plate and the mask during recording. Note that there is a strong zero-order beam during reconstruction that needs to be blocked to enhance the spot pattern contrast in the imaging sensor, as shown in Fig. 1(a). Using the in-line holography scheme, the focal length can be adjusted easily, and a large area of apertures in the mask can be recorded. The effective NA of the recording is ultimately limited by the resolution of the holographic material. Our holographic plate has a resolution of more than 3000 lines/mm , which corresponds to a maximum NA of 0.8 . The focus grid was observed under a microscope to measure the focus spot size. Figures 2(d)–2(f) show microscope images, using a $60\times$ objective, of spots from different region of the focus grid, as indicated in Fig. 2(c). The FWHM spot size was measured to be $0.65\text{--}0.80 \mu\text{m}$ (average of $0.74 \mu\text{m}$). The effective NA was ~ 0.36 , and the Rayleigh range is $\sim 2.3 \mu\text{m}$. The deviation of the experimental NA from the theoretical maximum NA is attributable to recording and developing imperfections. The nonuniform spot intensities of different focus spots were compensated by a normalization procedure during data processing. Note that the spot size in the x direction is larger than that in the y direction. The asymmetric shape of the spot was due to slight misalignment of the mask and holographic plate during the recording process.

The simplicity of this recording scheme and its robustness are important, as the method can be used to create

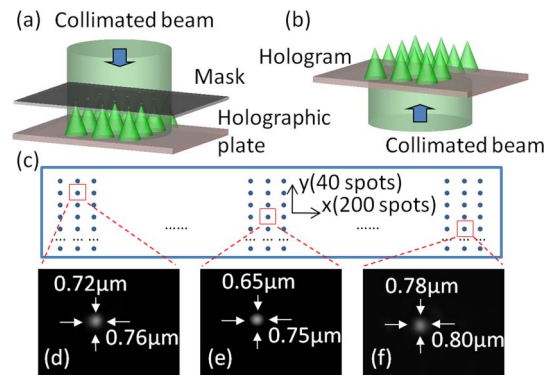


Fig. 2. (Color online) (a) In-line holographic recording scheme for making the hologram, (b) generation of focus grid illumination by holographic reconstruction using the hologram, (c) schematic of the focus grid, and (d)–(f) observation of focus spots from different regions of the focus grid, as indicated in (c), under a microscope using a $60\times$ objective.

large format and good quality light-spot-grid holograms. At this point, it is also worth noting that there are other ways to implement focus grid illumination, e.g., by using a microlens array [8]. The challenge of using a microlens array lies in the fact that, to maintain a reasonable NA and high focus-light-spot density, the focal length would have to be very short. For example, for a spacing of $30\text{ }\mu\text{m}$ and NA of 0.36, the microlens would have a diameter of $30\text{ }\mu\text{m}$ and a focal length of $\sim 40\text{ }\mu\text{m}$. Aside from fabrication issues related to the difficulty of implementing such small lenses and short focal lengths with good focusing quality, the short focal length is also inconvenient for sample handling. In comparison, our hologram had a much longer focal length of 6 mm. This difference is attributable to the fact that the effective lenses in the hologram can overlap each other, while microlenses simply cannot overlap in a microlens array. In fact, the extent of overlap for our prototype was remarkable. In our prototype, the holographic “lenses” were effectively 4.3 mm in diameter, while the lens-center spacing was $30\text{ }\mu\text{m}$.

To test our prototype system, we acquired images of a U.S. Air Force target and a lily anther microscope slide, as shown in Fig. 3. Figure 3(a) shows the wide FOV image of the U.S. Air Force target with effective FOV indicated by a dashed rectangle. Figure 3(b) shows the expanded view of the region indicated in Fig. 3(a), which contains the smallest feature size with a line width of $2.2\text{ }\mu\text{m}$ (group 7, element 6). Figure 3(c) shows the wide FOV image of the lily anther. Many distinct features, such as carpel, microspore, and petal, of the lily anther can be seen in the image. Small features can also be discerned, as demonstrated in Fig. 3(d), where an expanded-view image of the rectangle area indicated in Fig. 3(c) is shown. We can see that our system can render a wide FOV image and still provide good resolution. The shadow artifacts that are apparent in Fig. 3(b) were caused by crosstalk among the projected transmissions of the light spots. Light spots that were close to the feature edges tend to diffract strongly and introduce light onto regions of the camera that are sampling other spots. These systemic artifacts can be iteratively corrected via postimaging processing. We also note that scan motion nonuniformity ($\sim 0.8\text{ }\mu\text{m}$) is the cause of the image jitter along the scan direction, as can be seen in some horizontal bars. This issue can be solved by employing a more uniform linear actuation system.

Our HSM prototype actually operates in a sub-Nyquist sampling regime. To render full images at the fundamental resolution limit set by the spot size, the sampling increment for both directions should be halved. This can be accomplished by choosing a tilt angle θ of 0.0125 rad and using a scanning speed v of 6666 frames/s. Our achieved resolution with the demonstration operating parameters was $1.5\text{ }\mu\text{m}$; this is why we were able to discern the smallest individual scale bars (feature width = $2.2\text{ }\mu\text{m}$) in Fig. 3(b).

We note that our system does not contain feedback systems (common in commercial FOV systems) for keeping the sample in focus during scanning. We believe that our HSM design can potentially allow us to solve the axial focus control issue by a different means—by using the hologram to instead project a grid of finite Bessel beams [9], we can potentially image nonflat samples without requiring focus tracking. Finally, we note that the HSM can

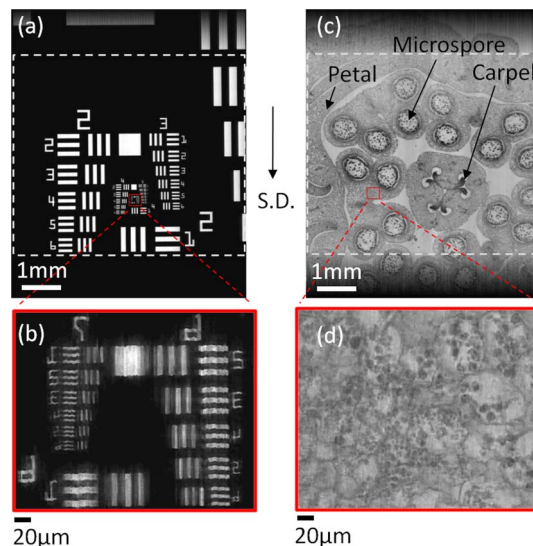


Fig. 3. (Color online) (a) Wide FOV image of a U.S. Air Force target, with an effective FOV of $6\text{ mm} \times 5\text{ mm}$, as indicated in the large dashed rectangle, (b) expanded view of the smallest feature (groups 6 and 7) of the target, as indicated in (a), (c) wide FOV image of a lily anther, with an effective FOV of $6\text{ mm} \times 5\text{ mm}$, as indicated in the large dashed rectangle, and (d) expanded view of the small rectangle area as indicated in (c). S.D., scanning direction.

potentially collect fluorescence images by simply inserting the appropriate filter.

In summary, we have shown a wide FOV microscope system based on holographic focus grid illumination. The use of focus grid illumination can effectively provide wide FOV and high-resolution microscopy imaging. We have demonstrated the principle by making a prototype system with an FOV of $6\text{ mm} \times 5\text{ mm}$ and an acquisition time of 2.5 s. The resolution is fundamentally limited by the spot size—our demonstrated average FWHM spot diameter was $0.74\text{ }\mu\text{m}$. The prototype system was used to image a U.S. Air Force target and a lily anther for capability testing.

This work is supported by Department of Defense grant W81XWH-09-1-0051. The authors acknowledge Richard Cote and Ram Datar from the University of Miami for helpful discussions.

References

1. M. Oheim, *Br. J. Pharmacol.* **152**, 1 (2007).
2. J. Ho, A. V. Parwani, D. M. Jukic, Y. Yagi, L. Anthony, and J. R. Gilbertson, *Hum. Pathol.* **37**, 322 (2006).
3. W. B. Xu, M. H. Jericho, I. A. Meinertzhagen, and H. J. Kreuzer, *Proc. Natl. Acad. Sci. USA* **98**, 11301 (2001).
4. S. Seo, T. W. Su, D. K. Tseng, A. Erlinger, and A. Ozcan, *Lab Chip* **9**, 777 (2009).
5. X. Q. Cui, L. M. Lee, X. Heng, W. W. Zhong, P. W. Sternberg, D. Psaltis, and C. H. Yang, *Proc. Natl. Acad. Sci. USA* **105**, 10670 (2008).
6. W. H. Liu and D. Psaltis, *Opt. Lett.* **24**, 1340 (1999).
7. F. Kalkum, S. Broch, T. Brands, and K. Buse, *Appl. Phys. B* **95**, 637 (2009).
8. C. H. Sow, A. A. Bettiol, Y. Y. G. Lee, F. C. Cheong, C. T. Lim, and F. Watt, *Appl. Phys. B* **78**, 705 (2004).
9. J. Durnin, J. J. Miceli, and J. H. Eberly, *Opt. Lett.* **13**, 79 (1988).